Key Points:

- Three presumed periglacial landforms (thermal contraction polygon, fractured mound, brain terrain) show similar distributions at 38°–42°N on Mars
- Their distribution corresponds well with the distribution of ice-exposing craters and the model-generated annual water ice budget on Mars
- Polygonal terrains were classified by shape, and the large-sized mixture type was interpreted as formed by the sub-surface ice degradation

Author Contributions:

Conceptualization: Hitoshi Hasegawa, Goro Komatsu, Yasuhito Sekine
Data curation: Takaki Sako
Funding acquisition: Hitoshi Hasegawa
Investigation: Takaki Sako, Hitoshi Hasegawa
Methodology: Hitoshi Hasegawa, Trishit Ruj
Project administration: Hitoshi Hasegawa
Supervision: Hitoshi Hasegawa
Validation: Hitoshi Hasegawa, Trishit Ruj, Goro Komatsu, Yasuhito Sekine
Visualization: Takaki Sako

The Periglacial Landforms and Estimated Subsurface Ice Distribution in the Northern Mid-Latitude of Mars

Takaki Sako[1,2], Hitoshi Hasegawa[1] , Trishit Ruj[2] , Goro Komatsu[3,4] , and Yasuhito Sekine[5,6,7]

[1]Faculty of Science and Technology, Kochi University, Kochi, Japan, [2]Institute for Planetary Materials, Okayama University, Tottori, Japan, [3]International Research School of Planetary Sciences, Università d'Annunzio, Pescara, Italy, [4]Planetary Exploration Research Center, Chiba Institute of Technology, Chiba, Japan, [5]Earth-Life Science Institute (ELSI), Institute of Science Tokyo, Tokyo, Japan, [6]Institute of Nature and Environmental Technology, Kanazawa University, Kanazawa, Japan, [7]Planetary Plasma and Atmospheric Research Center, Tohoku University, Sendai, Japan

Abstract Subsurface ice in the mid-latitude regions is a significant water inventory on present-day Mars, and their volume and distribution are thought to have varied due to the orbitally induced paleoclimatic changes. Using high-resolution satellite images, the present study explores the distributions of three presumed periglacial landforms (thermal contraction polygons, fractured mounds, and brain terrains) that could provide evidence for the present-day subsurface ice distribution in the northern mid-latitude (30°–42°N). We identified the three periglacial landforms concentrated within the regions of 0°–40°E, 60°–100°E, and 160°–210°E in the latitude of >33°N. Their distributions are in agreement with the occurrence of fresh ice-exposing craters and the estimated area of high annual water ice budget obtained by the general circulation model, reflecting the present-day subsurface ice distribution. We further classified the thermal contraction polygons into five types based on their morphology, and investigated various distribution patterns for each type. Among them, high-centered polygons are the most abundant type in the survey area, whereas low-centered polygons are less prominent and observed only at >38°N. The large-sized mixture polygons, which were only found in certain areas of 57°–92°E, are distributed in areas where the atmospheric model indicates that the highest annual water ice budget occurred during the past high-obliquity period, but that the water ice budget has decreased during the present-day low-obliquity condition. These findings, along with insights from possible terrestrial analogs in the Arctic Archipelago and northern Canada, suggest that regions where large-sized mixture polygons formed contained significant amounts of water ice in the past, but have undergone intense degradation over time.

Plain Language Summary How much water ice exists in the subsurface of Mars? Where is it currently distributed? How has its distribution varied with climate change from the past to the present? The answers to these questions are important for understanding the past and present-day hydrological cycle and habitability of Mars. One of the ways to infer the existence of invisible subsurface ice is to use periglacial landforms, which form where the surface topography is deformed due to the presence of subsurface ice. In this study, we explored the distributions of these periglacial landforms in the mid-latitude of Mars using high-resolution satellite images. The results indicate that the periglacial landforms are distributed in areas where ice tends to accumulate in the present-day Martian climate as obtained from climate model simulation. Furthermore, we found characteristic landforms formed by the degradation of subsurface ice in areas where large amounts of ice were likely deposited in the past Martian climate but decreased due to subsequent climate change.

1. Introduction

With the availability of comprehensive global coverage, satellite data show extensive evidence of Amazonian glaciation and glacial landforms in the mid-latitudes (30°–60°) in both hemispheres of Mars (Brough et al., 2016, 2019; Dickson et al., 2012; Head et al., 2003; Levy et al., 2014; Mangold, 2005). The evidence from glacial landforms and atmospheric models suggests that the locations of water ice accumulation have changed significantly due to obliquity-induced climate changes (Laskar et al., 2004; Madeleine et al., 2009; Fassett et al., 2014; Dickson et al., 2012). Fresh ice-exposing craters further indicate that a substantial amount of water ice have been preserved as frozen regolith in the present-day Martian mid-latitudes (Dundas et al., 2018, 2021; Posiolova et al., 2022). However, it is still uncertain exactly where the subsurface ice exists in the present-day Martian

Writing – original draft: Takaki Sako,
Hitoshi Hasegawa
Writing – review & editing:
Hitoshi Hasegawa, Trishit Ruj,
Goro Komatsu, Yasuhito Sekine

mid-latitudes, and how the volume and location of the subsurface ice have changed from the past high-obliquity period to the present.

The Subsurface Water Ice Mapping (SWIM) project aims to reconstruct the present-day subsurface ice distribution by integrating orbital data sets, such as radar data analysis and water equivalent hydrogen detection, along with the distribution of glacial landforms (Morgan et al., 2021). Recently, the SWIM project released an updated version of the ice consistency map that combines the distributions of periglacial landforms (i.e., thermal contraction polygon). However, the original data on the distributions of periglacial landforms are not publicly released, nor is the algorithm for how the ice consistency map was derived from the distributions of glacial and periglacial landforms, radar data, and hydrogen detection.

Landforms interpreted to be periglacial [for example, thermal contraction polygons, pingos (fractured mounds)] are distributed widely in the Martian mid-to-high-latitudes (de Pablo & Komatsu, 2009; Dundas & McEwen, 2010; Levy et al., 2009a, 2010a; Mangold, 2005; Marchant and Head, 2007; Seibert & Kargel, 2001; Soare et al., 2005). Since these periglacial landforms on Earth are developed in permafrost regions such as Alaska, Canada, Siberia, and Antarctica (e.g., Burr et al., 2009; Jones et al., 2012; Liljedahl et al., 2016; Marchant and Head, 2007; Soare et al., 2011; Soare et al., 2020), the equivalent landforms on Mars are also considered to reflect the existence of ground ice at present or recent past.

The polygons of probable thermal contraction origin are a few to dozen meters in size on Mars, and they can be observed clearly in images captured by the HiRISE (High-Resolution Imaging Science Experiment; McEwen et al., 2007). Levy et al. (2009a, 2010a) demonstrated that thermal contraction polygons are symmetrically distributed within the latitude range between 30° and 80° in both hemispheres. Pingos (ice-cored hills) are also important periglacial landforms that indicate the existence of ground ice (Burr et al., 2009; Grosse & Jones, 2011; Jones et al., 2012). HiRISE observations indicate the presense of fractured mounds in the 30°–50°N range of Utopia Planitia, which are interpreted as pingos (de Pablo & Komatsu, 2009; Dundas & McEwen, 2010; Soare et al., 2005, 2013, 2020). Brain terrains, characterized by surface textures resembling the human brain, are commonly found within craters at mid to high latitudes on Mars. Since brain terrains are often associated with glacial landforms (Squyres, 1979; Squyres and Carr, 1986), it has been thought that brain terrains were formed by glacial processes, having subsurface ice at the present-day (Levy et al., 2009b). On the other hand, some studies suggest the possible involvement of periglacial process for its formation (Cheng et al., 2021a; Mangold, 2003; Mellon et al., 2008). Therefore, complex mechanisms such as combined glacial and periglacial processes have been suggested as the origin of brain terrain (Baker et al., 2010; Cheng et al., 2021a; Levy et al., 2009b; Mangold, 2003; Mellon et al., 2008; Sinha & Vijayan, 2017).

While there have been studies (e.g., Bina & Osinski, 2021; Dundas & McEwen, 2010; Levy et al., 2009a, 2010a; Mangold, 2005) that investigated these presumed periglacial landforms independently (thermal contraction polygons, fractured mounds, and brain terrains) on Mars, the previous studies did not explore the relationships among their distributions. Examining the distributions of these landforms in the 30°–42°N range, where the icy and non-icy regions likely meet, is essential for understanding the subsurface ice volume and the history of water and ice on Mars. This region is also key for observing changes in the subsurface ice distribution from the past high-obliquity period to the present, as it may preserve relict landforms from earlier ice development phases.

In this study, we investigated 4,793 HiRISE images available for the northern hemisphere mid-latitude (30°–42°N) on Mars, where the southern limit of subsurface ice is thought to be positioned. We explored those HiRISE images and evaluated the relationships among the distributions of thermal contraction polygons, fractured mounds, and brain terrains (Figure S1 in Supporting Information S1). We then compared the results with the distributions of recent ice-exposing craters (Dundas et al., 2021; Posiolova et al., 2022), glacial landforms [Lobate Debris Aprons (LDA), Linear Valley Fill (LVA) and Concentric Crater Fill (CCF)] (Fasset et al., 2014; Levy et al., 2014; Souness et al., 2012), climate model results (Daerden et al., 2019; Forget et al., 1999; Madeleine et al., 2009; Pál et al., 2019), and the subsurface ice consistency map obtained by the SWIM project (Morgan et al., 2021). We further discuss the possible causes of the periglacial landform distributions, the inferred changes from the past high-obliquity period, and estimate the present-day subsurface ice distribution of the northern mid-latitudes on Mars, which is also crucial as a water resource of future human exploration.

2. Materials and Methods

We investigated the distributions of three presumed periglacial landforms (thermal contraction polygons, fractured mounds, brain terrain) by observing all HiRISE images currently available in the 30°–42°N latitude band (Figure S1 in Supporting Information S1; Table S1 in Supporting Information S1; Sako et al., 2024). Considering the relatively small dimensions of these landforms (sizes of fractured mounds are about tens to hundreds meters, while sizes of polygonal terrains are much smaller, ranging from 5 to 20 m in size), HiRISE images (30 cm/pixel) are the only competent data to identify them. Unlike the global coverage CTX (Context Camera; Malin et al., 2007) images, HiRISE covers only 5% of the survey area. Nevertheless, we used the HiRISE images as it is difficult to identify 10-m scale landforms with the CTX-scale resolution (6 m/pixel). The spatial distribution of the HiRISE images is mostly uniform across the study regions, although there are some pockets with marginally sparser data, such as at 230°–250°E. We consider these perspectives in our interpretations.

We used ArcGIS 10.8 to map the periglacial landform distributions using the HiRISE images and investigated the surface roughness and micro-topography of the areas according to shadow measurements and incident angle information. The rim height relative to the center of polygonal terrains is estimated using the directions of solar irradiance described in the label files (.lbl). The distributions of each landform were plotted on the MOLA (Mars Orbiter Laser Altimeter; Smith et al., 2001) shaded relief (Figure S1 in Supporting Information S1). The points representing the polygonal terrains, fractured mounds, and brain terrains are placed at the center of each HiRISE image where the target landforms were observed. This procedure was necessary because mapping all topographic features individually is a brutally time-consuming process. The contiguity of these landforms is listed in Table S1 of Supporting Information S1. The HiRISE images in which we did not find the target geomorphology or we were unable to see the image clearly due to the dust storms are marked as "No specific terrain". The kilometer-scale giant polygonal terrains identified in Utopia Planitia (e.g., Buczkowski et al., 2012; Hiesinger and Head, 2000) are not included as our target geomorphology in this study since other processes (i.e., volcanic or tectonic origins) may have been responsible for their formation. The target periglacial landform types were identified by referring to the criteria described below.

2.1. Polygons

The polygonal terrains, which are normally square or hexagonal patterned ground, are common on Martian surfaces (Figure 1). Most of these terrains observed at mid-to high latitudes (>30°) have been hypothesized with periglacial thermal contraction origins (e.g., Levy et al., 2009a; Marchant and Head, 2007; Seibert & Kargel, 2001; Soare et al., 2011, 2014a). NASA's Phoenix lander, which landed in 2008 at a northern high-latitude site where polygonal terrain had developed, is reported to have found water ice several centimeters beneath the surface (Arvidson et al., 2008; Mellon, Arvidson, et al., 2009; Mellon & Malin et al., 2009). Furthermore, ice-exposing fresh impact craters have been reported from some polygonal landform sites (Dundas et al., 2021), which also supports the present-day existence of subsurface ice underneath the polygonal terrain.

On Earth, polygonal terrains commonly develop in permafrost regions, such as those identified in Alaska, Canada, Siberia, Mongolia and Antarctica. Since many of polygonal terrains have ice wedges at the polygon rims, they are commonly called ice-wedge polygons (Dafflon et al., 2016; Liljedahl et al., 2016; Marchant and Head, 2007; Matsuoka, 2011; Matsuoka et al., 2018; Murton, 2013). Ice-wedge polygons on Earth are developed through the following processes: (a) cracking of periglacial terrain during winter, (b) infilling of the cracks by meltwater during spring or summer, (c) freezing of the water-filled cracks, and progressive formation wide and deep ice-wedges during winter. In near-surface ice-rich permafrost regions such as Tuktoyaktuk Coastlands in northern Canada, polygons are often formed by ice-wedges as a result of freeze-thaw cycles influenced by meltwater influence (Soare et al., 2011). In contrast, polygons also develop in cold, dry permafrost environments such as the Dry Valleys of Antarctica, where liquid water is typically absent (Marchant et al., 2002; Sletten et al., 2003). Here, polygons form through thermal contraction cracking, accompanied by the sublimation of buried ice. Then, cracks are frequently filled with wind-blown sand, resulting in the formation of sand-wedge polygons. Thus, although some polygonal terrains in Antarctica do not show clear signatures of ice-wedges, it is possible that ground ice was involved in their formation process. Thus, in this study, we focused on relating the distributions of periglacial landforms on Mars to the presence of subsurface ice in the present or recent past.

Previously, using HiRISE images, Levy et al. (2009a, 2010a) investigated polygonal terrains between 30° and 80° latitudes on Mars and classified them into seven types, including High-Relief Polygon, Flat-Top Small Polygon,
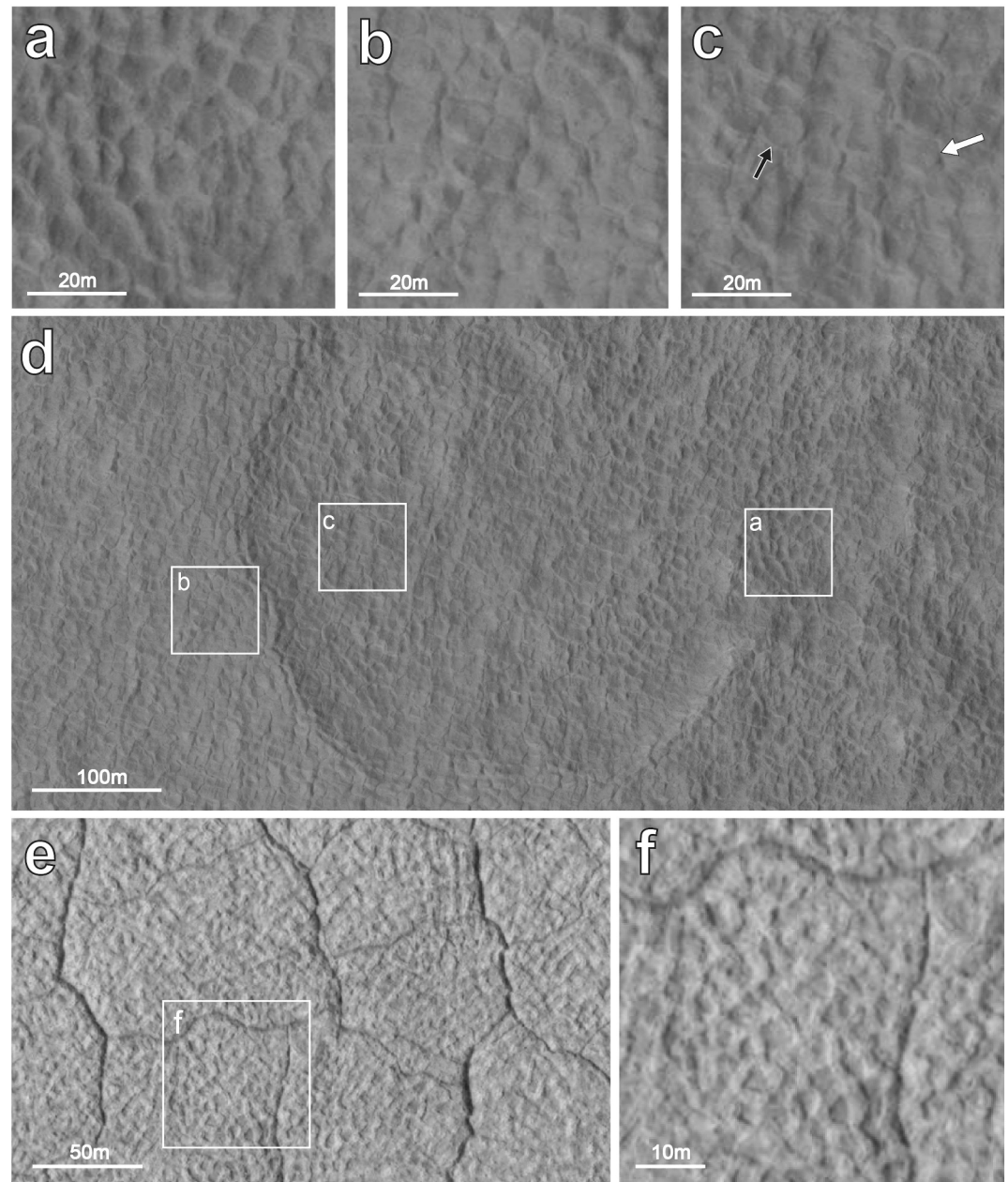
Figure 1. The HiRISE images of several polygonal terrains, LCPs (a), HCPs (b) and LHTs (c) in western Utopia Planitia (ESP_016705_2215; 40.972°N, 123.371°E). Black arrow indicates LCPs, while white arrow indicates HCPs. (d) Location of the three types of polygons within Scalloped Depressions. (e) LMPs in the western Utopia Planitia (ESP_055026_2220; 41.915°N, 81.96°E). (f) Small polygons (5–10 m diameter) found within LMPs.

Irregular Polygon, Subdued Polygon, Gullygon, Peak-Top Polygon, and Mixed Center Polygon (Table 1). On the other hand, in our study, following the nomenclature commonly used for polygonal terrains on Earth, the terms "Low-Centered Polygon (LCP)" and "High-Centered Polygon (HCP)" are used to describe the relative height of the polygon's edge or rims to the center (Soare et al., 2014a, 2014b).

We classified the polygonal terrains into the following five types: LCP, HCP, LCP-HCP transition (LHT), Polygon in Scalloped depression (PSD), and Large-sized Mixture Polygon (LMP). Peak-Top Polygon of Levy et al. (2009a) corresponds to HCP in this study. The Mixed Center Polygon of Levy et al. (2009a) is further subdivided into HCP, LCP, LHT, and PSD. LMP is a new classification in this study. Flat-Top Small Polygon, Subdued Polygon, and

Table 1
Comparison of the Polygon Type Classification Between Levy et al., 2009a and This Study

Levy et al., 2009a	This study
Peak-Top Polygon	High-Centered Polygon (HCP)
Mixed Center Polygon	High-Centered Polygon (HCP)
	Low-Centered Polygon (LCP)
	LCP-HCP Transition (LHT)
	Polygon in Scalloped Depression (PSD)
not defined	Large-sized Mixture Polygon (LMP)

Gullygon were not found in our survey area. The correlation between the classifications by Levy et al. (2009a) and our study is shown in Table 1.

2.1.1. Low-Centered Polygons

LCPs (Figure 1a) are 10–20 m in diameter with a raised rim and a depressed center. The raised rim of the LCP has a distinct crack, which can be formed by repeated thermal cracking of ice wedges. Their shapes are nearly hexagonal or squares, showing homogeneous size and shapes similar to the shape of the HCPs. On Earth, LCP-type polygons are interpreted to hold more ice than HCPs do, and transformation from LCPs to HCPs due to degradation over several decades has been observed (Lilijedahl et al., 2016). In our survey area, there was no region where only the LCP existed alone, and many of the observed LCPs were contiguous with HCPs.

2.1.2. High-Centered Polygons

HCPs (Figure 1b) are polygons with raised centers and lowered rims (troughs) with diameters ranging from 5 to 20 m. Their shapes are nearly hexagonal or square, showing homogeneous size and shapes. The HCP-type polygon on Earth is formed by degradation and transformation from the ice-wedge-rich LCP type (Dafflon et al., 2016; Lilijedahl et al., 2016). Soare et al. (2021) demonstrated an increase in the abundance of LCPs compared with HCPs toward the pole in Utopia Planitia (40°–50°N; 100°–125°E). This suggests that there is less ice where HCPs form than where LCPs form, which is comparable to the terrestrial case.

2.1.3. HCP-LCP Transitions

LHTs (Figure 1c) are transitional forms where both LCPs and HCPs are found. We have distinguished LHTs fpr locations where most of the polygons are HCPs in shape, but where LCP-type polygons are also interspersed. In general, LHTs are mostly associated with scalloped depressions.

2.1.4. Polygons in Scalloped Depression (PSD) (Figure 3B)

Scalloped depressions (Figure 1d) are shell-shaped depressions with a diameter ranging from several hundreds of meters to kilometers, and are widely identified in Utopia Planitia. They have been interpreted as a feature formed due to ice degradation (Dundas et al., 2015; Séjourné et al., 2011, 2019; Soare et al., 2007, 2011; Ulrich et al., 2011). The presence of scalloped depressions indicates an ice-rich stratified sedimentary permafrost layer (approximately 80 m in thickness), containing excess ice (Séjourné et al., 2019). In some regions, both HCPs and LCP (and LHTs) are distributed inside scalloped depressions; HCPs are located on the equatorial slope while LCPs and LHTs tend to be located in the polar slope concavity. The polygons on the northern and northeastern sides of the depressions have bumpy surfaces and seem degraded, suggesting that the depression developed toward higher latitudes.

2.1.5. Large-Sized Mixture Polygons (LMPs) (Figure 3A)

The LMPs (Figure 1e) are characterized by a large polygon approximately 100 m in diameter, with smaller polygons (diameter about 5–10 m; Figure 1f) within the large polygon. The smaller polygons have raised rims without cracks in the rim (Figure 1f), while larger polygons have valley rims (lowered edges). Previous studies (Costard et al., 2016; Costard & Kargel, 1995; Seibert & Kargel, 2001; Séjourné et al., 2019; Soare et al., 2011, 2021; Ulrich et al., 2011) also reported the occurrence of such large ~100 m size polygons in western Utopia Planitia, which they called the UP1 type. The Mixed center polygons of Levy et al. (2009a) differ from LMPs in that they are polygons with HCPs and LCPs coexisting in a scalloped depression (Table 1). The large-sized polygons in Utopia Planitia are thought to be formed in the past during higher obliquity conditions (Costard et al., 2016; Séjourné et al., 2019; Soare et al., 2021; Ulrich et al., 2011). Deep, elongated pits aligned along the N–S junction of polygonal margins are characteristics of the edges of LMPs (Séjourné et al., 2019; Soare et al., 2011). Since they are cut by the scalloped depressions, the LMP polygons are interpreted to be older in age (Ulrich et al., 2011).

2.1.6. Other Polygons

In addition to the polygonal terrains described above, we identified specific shapes of polygonal terrains similar to the desiccation-related polygons observed in dry salt lakes on Earth (e.g., Cheng et al., 2021b; Dang et al., 2018; Komatsu et al., 2007). They are generally rectangular or complexly polygonal in shape (Dang et al., 2018), and frequently located in areas with light-toned materials and chloride-bearing strata on Mars (El-Maarry et al., 2013, 2014; Osterloo et al., 2008). We named such terrains as Desiccation Polygons (DPs). Some DPs also show tortuous raised rims and sinuous crack types, and similar morphology has also been identified in the Qaidam Basin on Earth (Anglés & Li, 2017; Xiao et al., 2017). Some studies (Cheng et al., 2021b; Dang et al., 2018) have pointed to the possibility that features of thermal contraction patterns may also be found in the desiccation process, and it may be difficult to distinguish the two mechanisms based on the morphology alone. On the other hand, El-Maarry et al. (2013) suggest that polygonal terrains of more than 75 m in size cannot be formed solely due to thermal stresses, based on the fracture mechanisms of crack propagation in frozen soil under the present-day Martian climate conditions.

Therefore, in this study, we distinguish between DPs and periglacial thermal contraction polygons based on their size and geological classification (e.g., coexistence with light-toned materials and chloride-bearing deposits). Some polygonal terrains, which are difficult to distinguish between DPs and periglacial terrains, are included in the Irregular Polygons (IPs) and omitted from the discussion in this paper. IPs are unusual polygons that we cannot categorize in any of the other six types. For example, they include very small-sized (<5 m) and irregularly shaped polygons. The distribution of DPs and IPs was explored and shown in Supporting Information S1 (Table S1 and Figure S1 in Supporting Information S1), but is not discussed in this study.

2.2. Fractured Mounds

Fractured mounds are landforms with cracks developing on the top (Figure 4). The fractured mounds on Earth are known to be part of an evolutionary process of periglacial landforms called pingos. A pingo is a landform formed by lenticular ice cone growth beneath the mound (Grosse & Jones, 2011; Jones et al., 2012; Soare et al., 2005). The ice core beneath the mound can grow and become a high cone. After the growth of the ice core, cracks and fractures develop in the surface, and depressions are formed at the summit (Mackay, 1998, 1999; de Pablo & Komatsu, 2009; Soare et al., 2013, 2014b; Ishikawa & Yamkhin, 2016; Soare et al., 2020, 2021).

On Earth, two types of pingos have been identified: closed system (hydrostatic) and open system (hydraulic) (Soare et al., 2013, 2014b, 2020). Closed system pingos (CSPs) are perennial ice-cored mounds that develop on relatively deep and continuous permafrost (Soare et al., 2020). On the other hand, open system pingos (OSPs) form on discontinuous permafrost that are fed by external water supply (Soare, Conway, Dohm, et al., 2014). Both types of pingo can be distinguished by occurrence and associated landforms; for example, CSPs are often observed in regions where ambient temperatures have risen, "ice-rich" permafrost has been thermally destabilized, and thermokarst lakes have formed (Soare, Conway, Dohm, et al., 2014). In contrast, OSPs are often developed in areas associated with faults and glacial lobes.

On Mars, pingo-like features of fractured mounds have been found in many locations, including Utopia and Elysium Planitia (e.g., de Pablo & Komatsu, 2009; Dundas & McEwen, 2010; Soare et al., 2013, 2020). In previous studies, mound landforms with circular to slightly elongated shapes and cracks on the top were defined as fractured mounds, and we followed that criterion (Dundas & McEwen, 2010). Following the criteria from the previous study by Soare et al. (2014b, 2020), we classified fracture mounds within scalloped depressions as CSP-like fractured mounds (Figure 2a). In contrast, those associated with gullies and lobes or existing independently were classified as OSP-like fractured mounds (Figure 2b).

2.3. Brain Terrains

Brain terrain (Figure 3) is a specific landform developed in Martian mid-to-high latitudes, and the surface texture resembles a human brain-cell (Levy et al., 2009b, 2010b). Since brain terrain is often associated with glacial landforms such as LDA, LVF, and CCF deposits, which are found at latitudes higher than 30°N (Squyres, 1979; Squyres and Carr, 1986), it has been thought that brain terrains were formed by glacial processes, having subsurface ice at the present-day (Levy et al., 2009b). On the other hand, some studies suggested a possible involvement of periglacial process for its formation, including evidence near Phoenix landing sites
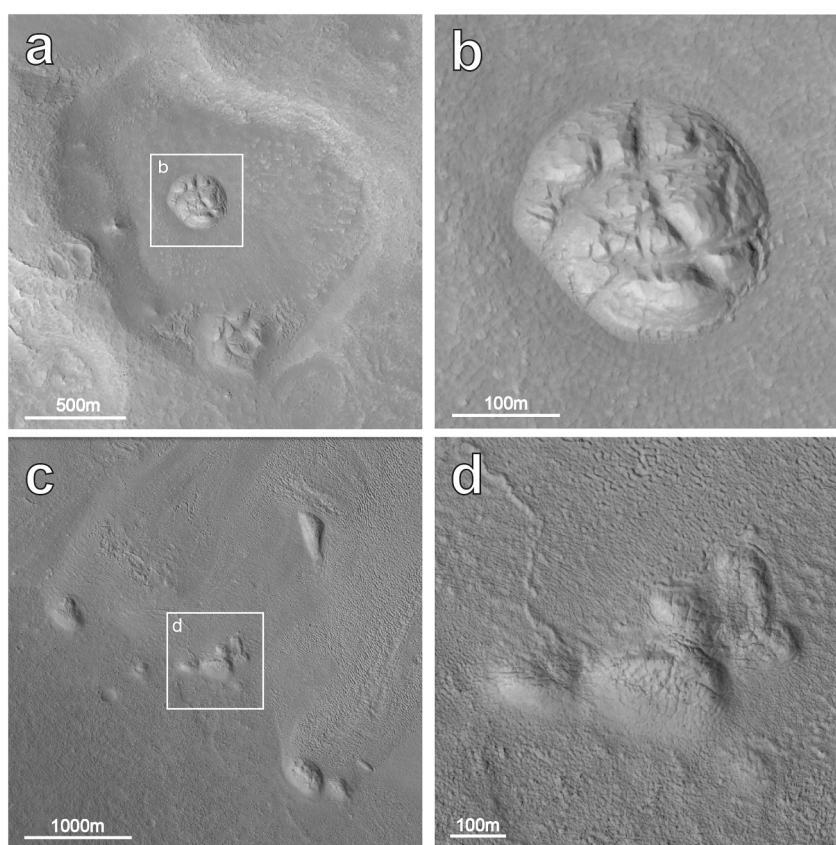
Figure 2. HiRISE images showing two types (CSPs and OSPs) of fractured mounds. (a) CSP-like fractured mounds within the depressions in western Arabia Terra (ESP_051230_2200; 39.8122°N, 39.6283°E). (b) Enlarged mound image of (a). (c) OSP-like fractured mounds associated with glacial landforms in western Arabia Terra (ESP_019768_2220; 41.5891°N, 18.4233°E). (d) Enlarged mound image of (c).

(Cheng et al., 2021a; Mangold, 2003; Mellon et al., 2008). Given the presence of abundant ring-mold craters (Kress & Head, 2008) on the surface of brain terrains, and observations of radar sounding data collected by the SHARAD (SHAllow RADar) (Holt et al., 2008; Plaut et al., 2009), the presense of present-day subsurface ice is suggested (Baker et al., 2010; Sinha & Vijayan, 2017). Thus, although the formation mechanisms of the brain terrains are debated, complex mechanisms such as a combined glacial and periglacial processes have been suggested as the origin of brain terrain (Baker et al., 2010; Cheng et al., 2021a; Levy et al., 2009b; Mangold, 2003; Mellon et al., 2008; Sinha & Vijayan, 2017). Therefore, in this study, we explored the relationship between the distribution of the brain terrains and the other periglacial landforms such as thermal contraction polygons and fractured mounds.

3. Observation Results

3.1. 0°–60°E (Western Arabia Terra)

In this area (Figure 4), polygonal landforms such as LCPs (Figure 5a), HCPs (Figure 5b), fractured mounds (Figure 5c), and brain terrain (Figure 5d) are distributed particularly from 35° to 42°N and 0°–40°E. On the other hand, the distribution of the three periglacial landforms in the 40°–60°E longitude range is restricted to latitudes higher than 38°N. This less-pronounced zone corresponds to the area of relatively high topographic relief (Figure 4). In this area, the three periglacial landforms tend to be distributed inside of craters and bottom of channels (different from Gallygon of Levy et al., 2009a). Polygonal terrains are commonly observed in flat areas near the southern slope of the craters and at the channels.

HCPs are the common type of polygons in this region, with a diameter of about 10–20 m and homogeneous shapes of hexagon and square (Figure 5b). LCPs of about 10–20 m size are also found in two regions at around 40°N,
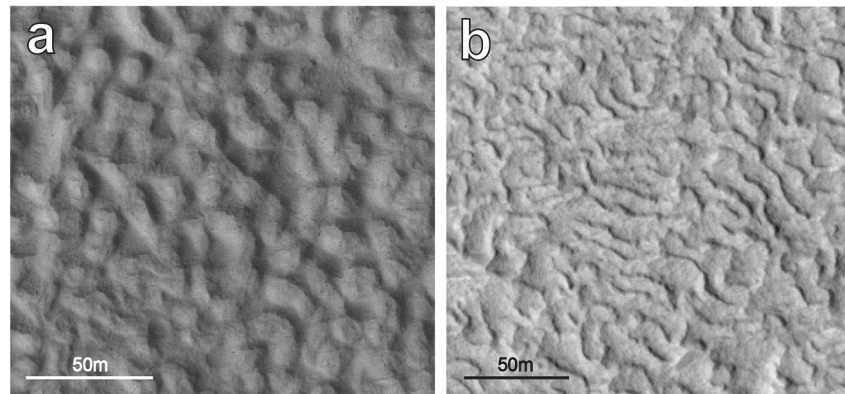
Figure 3. HiRISE images gallery showing Brain terrain in the study site. (a) Brain terrain in western Utopia Planitia (ESP_012751_2135; 33.414°N, 70.271°E). (b) Brain terrain in western Arabia Terra (ESP_052464_2190; 38.600°N, 189.946°E).

29°E and 39°N, 55°E (Figure 5a). LHTs are observed in one area of 42°N, 10°E. PSDs are identified from 0° to 7°E, 22–24°E, and 55°–60°E at latitudes generally higher than 40°N. LMP are characteristically distributed in the areas between 38° and 42°N and 57°–60°E.

3.2. 60°E to 120°E (Eastern Arabia Terra and Western Utopia Planitia)

In this area, HCPs with a diameter of about 10–20 m are present (Figure 6). LCPs are identified in only one HiRISE image, centered at 41°N and 120°E (Figure 7a). HCPs are sparsely distributed in the region between 38° and 42°N and 90°–120°E, where they coexist with fractured mounds and/or brain terrain (Figure 7b). CSP- and OSP-like fractured mounds are also observed (Figures 7c and 7d). One important characteristic of this region is the occurrence of LMPs (Figures 1e and 1f) in the region between 38° and 42°N and 70°–92°E. These are the only zones within the survey area where LMPs are concentrated. The LMPs consist of a mixture of large-sized polygons (about 100 m in diameter) and small polygons (about 5–10 m in diameter). The small polygons in
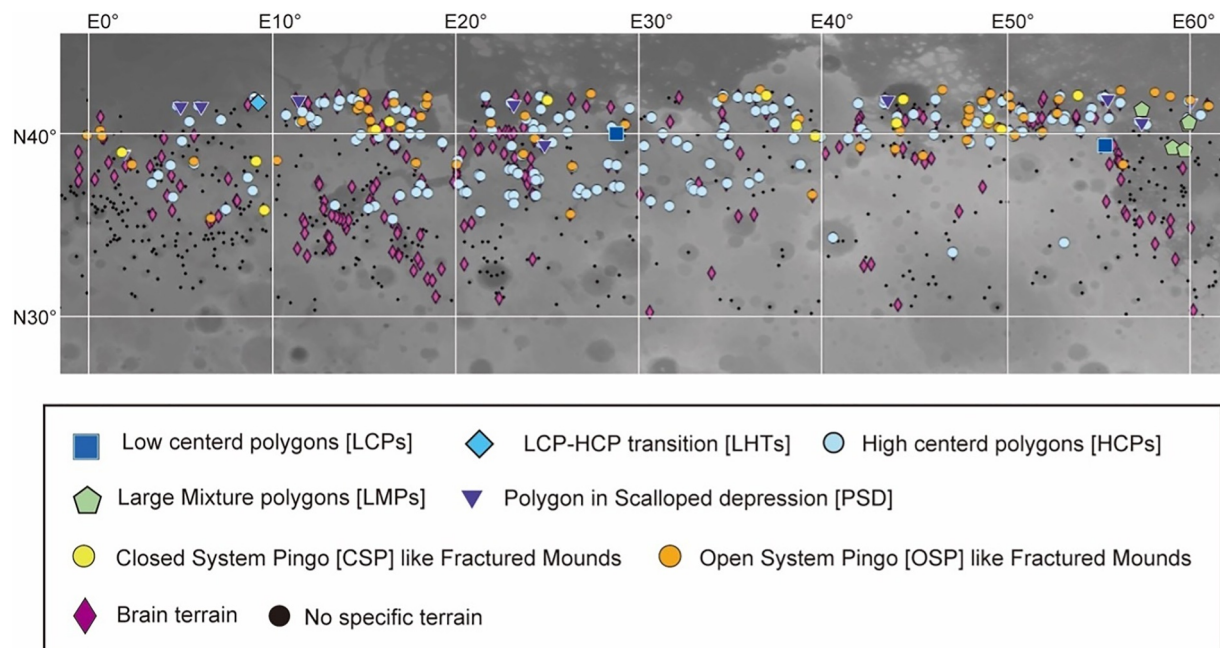

Figure 4. The distribution of target landforms from 0°E to 60°E. This area is on the west side of Arabia Terra. Between 0° and 30°E longitudinal band, thermal contraction polygons and fractured mounds are found in lower latitudes at around 35°N.
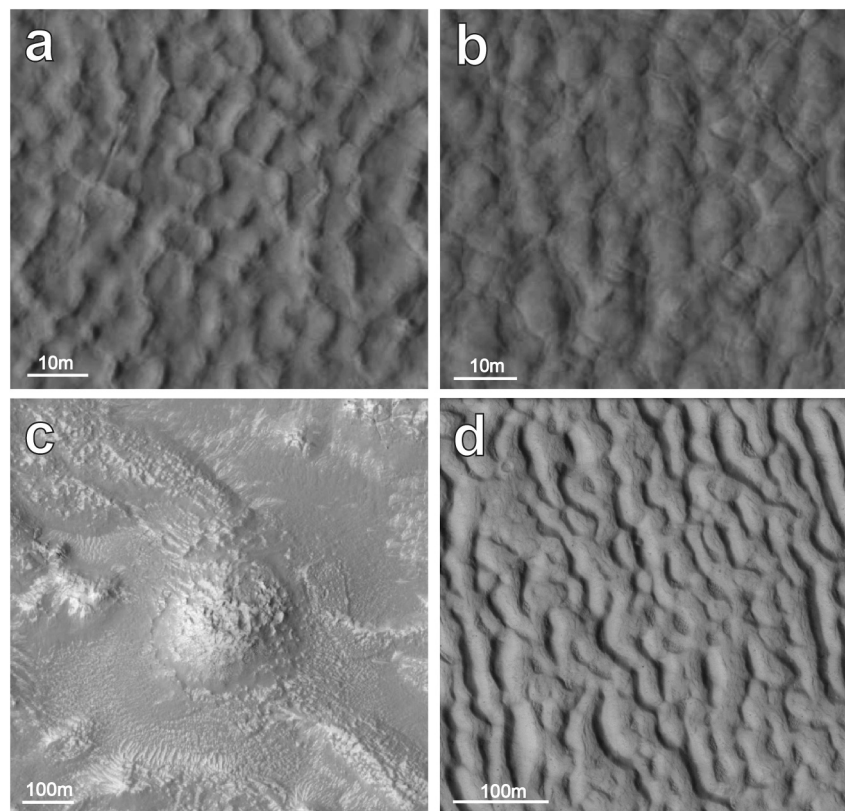
Figure 5. HiRISE images of characteristic landforms in 0–60°E, Arabia Terra. (a) LCPs of 10–20 m width (ESP_072398_2220; 41.478°N, 6.132°E). (b) HCPs of 10–20 m width (ESP_072398_2220; 41.478°N, 6.132°E). (c) CSP-like fractured mounds in western Arabia Terra (ESP_043227_2140; 33.53375°N, 12.9123°E). (d) Brain terrain and fractured mound in western Arabia Terra (ESP_046497_2195; 38.948°N, 22.6768°E).

LMPs have no cracks at the rim (Figure 1f). LMPs distributed around 42°N coexist with PSDs. It is noteworthy that the CSP-like fractured mounds are not observed in the LMP area.

3.3. 120°E to 180°E (Eastern Utopia Planitia and North of Elysium Mons)

In this area (Figure 8), LCPs (Figure 9a), HCPs (Figure 9b), CSP-like fractured mounds (Figure 9c), and brain terrain (Figure 9d) are sparsely distributed at latitudes ranging between 38° and 42°N. In the area of 120°–127°E, CCP and fractured mounds exist around ~40°–42°N, and only brain terrains are observed in the lower latitudes.
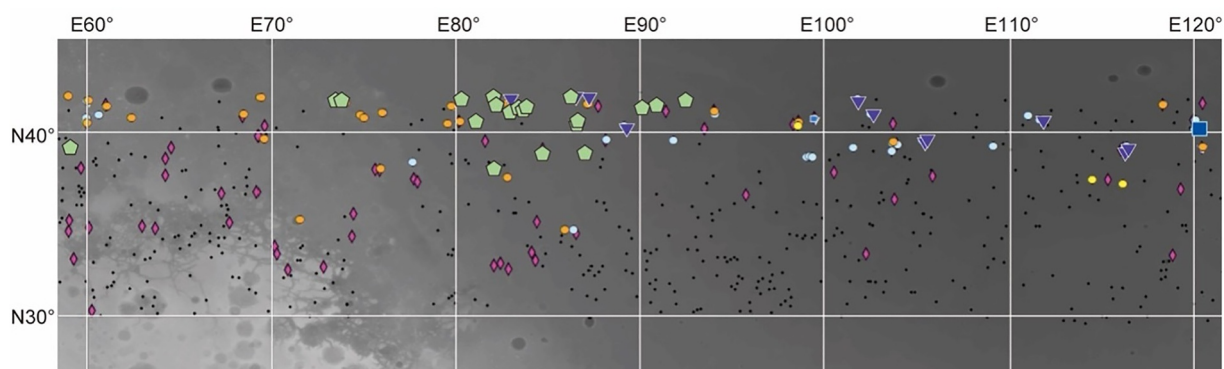

Figure 6. The distribution of target landforms from 60° to 120°E. This region corresponds to eastern Arabia Terra and Utopia Planitia. LMPs are particularly distributed in the region between 70° and 92°E. Symbol legends are shown in Figure 4.
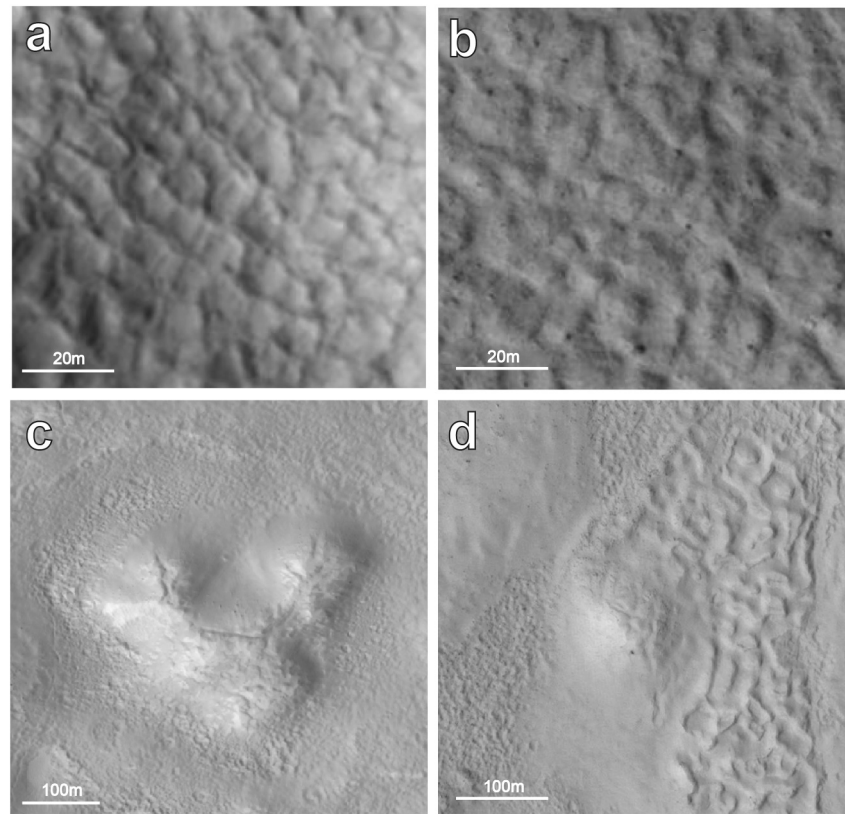
Figure 7. HiRISE images of characteristic landforms in 60°–120°E area (eastern Arabia Terra and western Utopia Planitia). (a) LCP with a diameter of about 10 m. The polygon rim is raised and has cracks (PSP_06908_2215; 41.178°N, 124.127°E). (b) HCP with a diameter of about 10–20 m (PSP_007001_2200; 39.482°N, 105.541°E). (c) CSP-like fractured mounds in western Utopia planitia (ESP_16191_2175; 37.0663°N, 116.229°E). (d) OSP-like fractured mounds associated with glacial landforms in western Utopia planitia (ESP_026041_2215; 41.373°N, 118.4455°E).

On the other hand, from 158° to 180°E, HCPs, brain terrain, and fractured mounds are more widely distributed down to ~35°N. Especially, brain terrain is densely concentrated in high altitude areas of Phlegra Montes around 160°–165°E. LCPs are identified in four HiRISE images at 120°E to 125°E (note that only two symbols are visible because they are distributed in very close images). All the LCPs in this region are distributed within scalloped depressions. These are the same as those listed in Table 1 of Soare et al. (2021). LHTs were seen in three images near 39°N at 172°E.
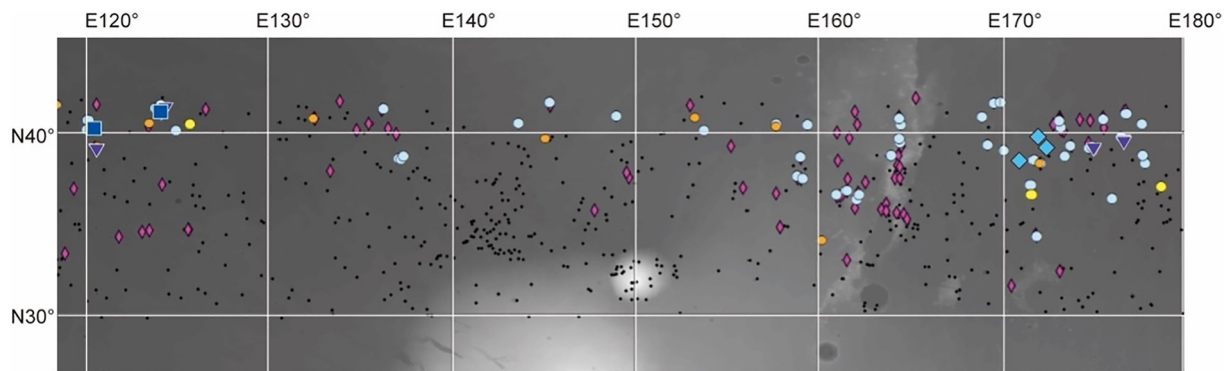

Figure 8. The distribution of target landforms from 120° to 180°E. This area is north of Elysium volcano, 120° to 130°E is Utopia Planitia, 160° to 180°E is Arcadia Planitia and Amazonis Planitia. This region is characterized by less periglacial landform distribution than longitudes of 0°–120°E. Symbol legends are shown in Figure 4.
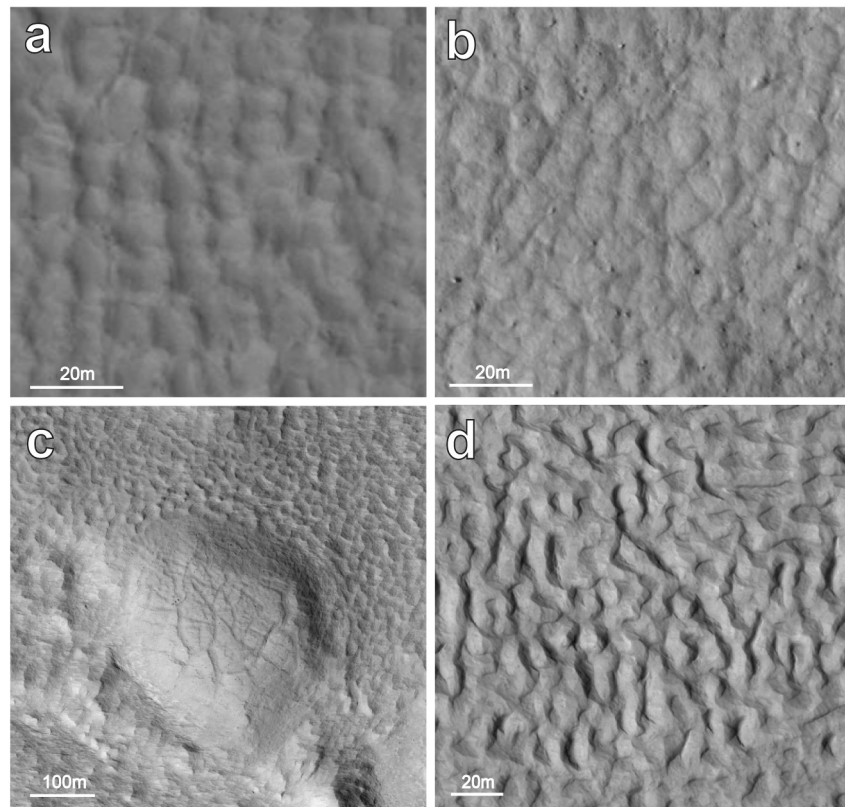
Figure 9. HiRISE images of characteristic landforms in 120°–180°E, eastern Utopia Planitia. (a) LCPs in northern Elysium mons. These polygons are about 10–20 m in diameter, hexagonal in shape, and uniform in size (ESP_045608_2205; 40.853°N, 173.263°E). (b) HCPs in northern Elysium mons. These polygons are about 10–20 m in diameter, hexagonal in shape, and uniform in size (ESP_019354_2170; 36.613°N, 162.265°E). (c) OSP-like fractured mounds in northern Elysium mons (ESP_046387_2200; 39.680°N, 145.128°E). (d) Brain terrain in North of Elysium Mons (ESP_078432_2170; 36.642°N, 162.351°E).

3.4. 180°E to 240°E (Amazonis Planitia, and Northern Olympus Mons)

Polygons, fractured mounds, and brain terrains are observed north of 35°N in the region from 180°E to 210°E (Figure 10). On the other hand, polygons and brain terrain are rarely found east of 210°E, although fractured mounds are sparsely distributed. HCPs (Figure 11a) are densely concentrated in the region between 35° and 42°N
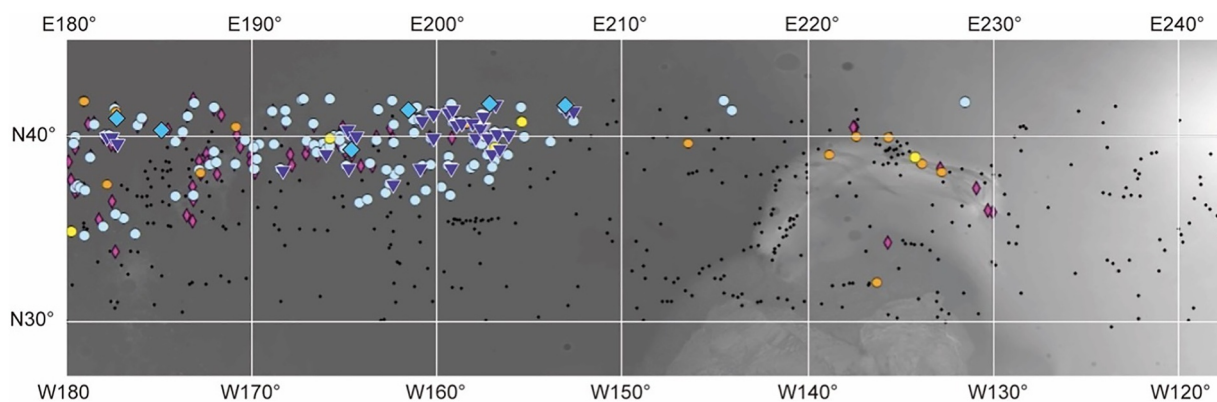

Figure 10. The distribution of target landforms from 180° to 240°E region. The depicted area corresponds to Arcadia Planitia and Amazonis Planitia, located north of Olympus Mons. In the western section of this region, specifically west of 210°E, there is a comparatively reduced occurrence of periglacial landforms. Symbol legends are shown in Figure 4.
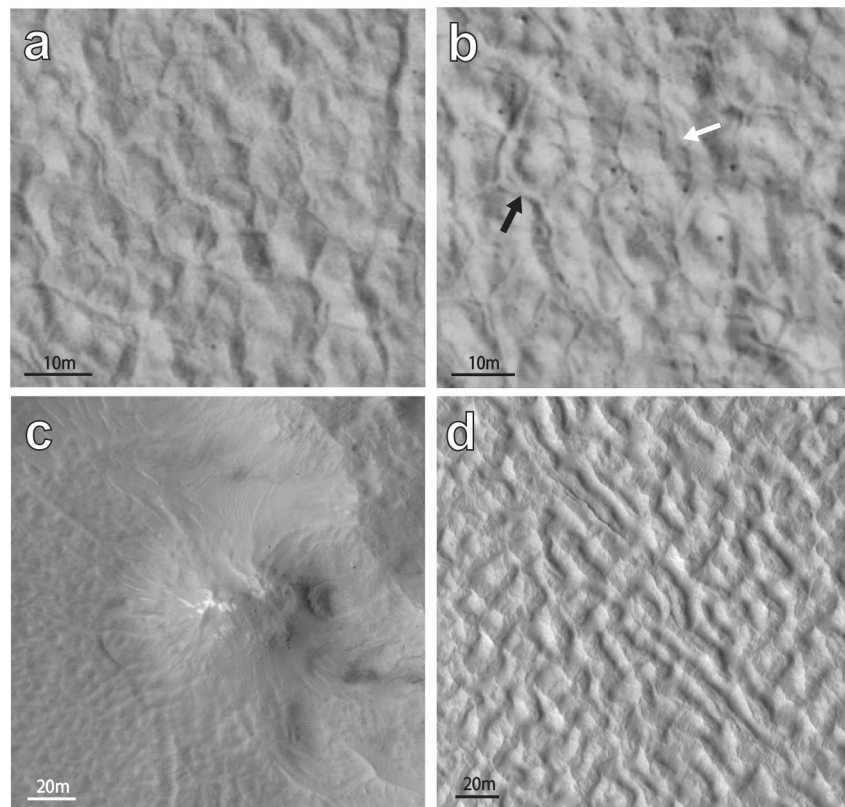
Figure 11. HiRISE images of characteristic landforms in 180°–240°E (Arcadia Planitia and Amazonis Planitia). (a) HCPs with a diameter of about 10–20 m (ESP_037655_2210; 40.560°N, 202.404°E). (b) LHTs with a diameter of about 10 m. LCPs are indicated by black arrows and HCPs by white arrows (ESP_015898_2225; 41.980°N, 194.221°E). (c) CSP-like fractured mounds in Amazonis Planitia (ESP_016848_2155; 34.9853°N, 180.206°E). This mound is located in a depression. (d) Brain terrains in Amazonis Planitia (ESP_063726_2155; 35.4524°N, 181.7855°E).

and 180°–210°E. LHTs (Figure 11b) are sparsely distributed at ~180°E− 210°E north of >38°N. Fractured mounds are both OSP- and CSP-types (Figure 11c). Scalloped depressions are particularly concentrated in the regions between 37° and 42°N and 194°–205°E. The distribution of brain terrain (Figure 11d) shows a zonal orientation in the SW–NE direction, extending from 182°E, 33°N to 193°E, 40°N (Hibbard et al., 2021).

3.5. 240°E to 300°E (Alba Mons and Tempe Terra)

The target periglacial landforms are only observed between 269° and 280°E and 293°–297°E (Figure 12). OSP-like fractured mounds (Figure 13a) and brain terrains (Figure 13b) are sparsely distributed mainly in the high latitude areas of >40°N.

3.6. 300°E to 360°E (Northern Chryse Planitia and Southern Acidalia Planitia)

Target periglacial landforms are rarely observed in this area (Figure 14). OSP-like fractured mounds (Figure 15a) and brain terrains (Figure 15b) are sparsely distributed at >40°N. Brain terrain is sparsely observed between 348° and 360°E.

4. Discussions

4.1. Distributions of Three Periglacial Landforms in the Northern Mid-Latitude (30°–42°N)

We identified the distributions of three presumed periglacial landforms, especially within the regions of 0°–40°E, 60°–100°E and 160°–210°E, for latitudes of >33°N (Figures 16a–16e; Figures 17a–17e). Conversely, these landforms have limited occurrences in the western hemisphere, particularly between 230° and 270°E and 280°–350°E. Notably, the areas featuring polygonal terrains, fractured mounds (especially CSP-type), and brain
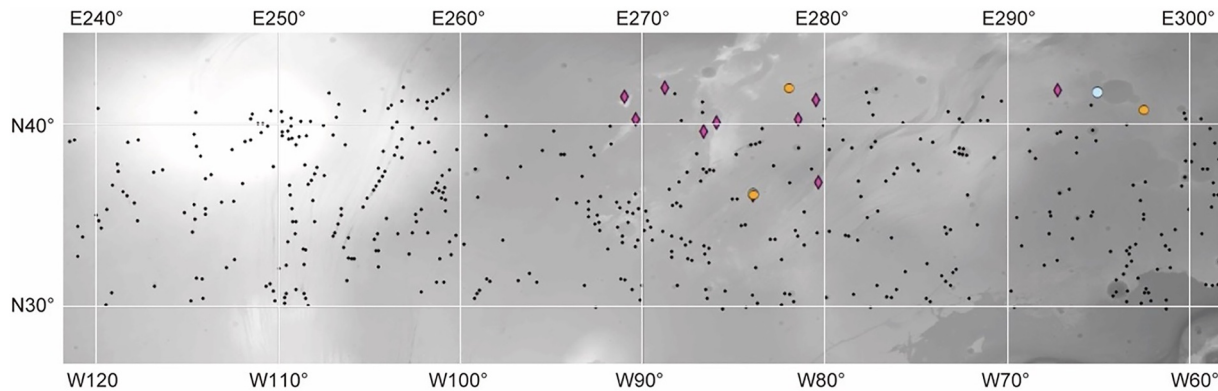
Figure 12. The distribution of target landforms from 240° to 300°E region. The depicted region corresponds to Tempe Terra, located north of Olympus Mons. Periglacial landforms exhibit limited distribution within this area. Symbol legends are shown in Figure 4.

terrain also align with areas exhibiting fresh impact craters exposing ice (Dundas et al., 2021; Posiolova et al., 2022; Figure 16f), which strongly supports the link between periglacial landforms and subsurface ice. Thus, it is highly likely that the existence of present-day subsurface ice plays an important role in the development of these three landforms.

The polygonal terrains also have distinct distribution patterns according to their morphology. HCPs are widespread across areas showing also the contiguity of the three periglacial landforms, except in the 60°–100°E region. It is noteworthy that LCPs and LHTs are distributed around 10°E, 30°E, 55°E, 100°E, 120°–124°E, 170°–173°E and 180°–208°E, closely corresponding to the areas with freshly ice-exposed craters (Dundas et al., 2021; Posiolova et al., 2022; Figure 16f). Conversely, the 57°–92°E region is dominated by LMPs (Figure 1e), while HCPs are less abundant and LCPs are absent. The occurrence of ∼100 m-sized polygons in this region is also noted by previous studies (Costard et al., 2016; Séjourné et al., 2019; Soare et al., 2021; Soare et al., 2011; Ulrich et al., 2011), and they are thought to have formed during the past high obliquity (>35°) periods. The existence of scalloped depressions truncating these large-sized polygonal terrains (Ulrich et al., 2011) also supports their older ages, such as during the high obliquity period (>5 Ma).

Smaller polygons within LMPs, ranging from 5 to 10 m in diameter and lacking cracks on the rims (Figure 1f), exhibit features similar to the morphology of the brain terrain. The absence of cracks on the rims may suggest that the raised rims formed as sand-wedges filled with wind-blown material (Murton et al., 2000; Ulrich et al., 2011). The raised rims were protected by the filled sand material, but the polygon centers were depressed by intense ice degradation (Levy et al., 2009b; Ulrich et al., 2011). Thus, the smaller polygons in the LMPs may have been
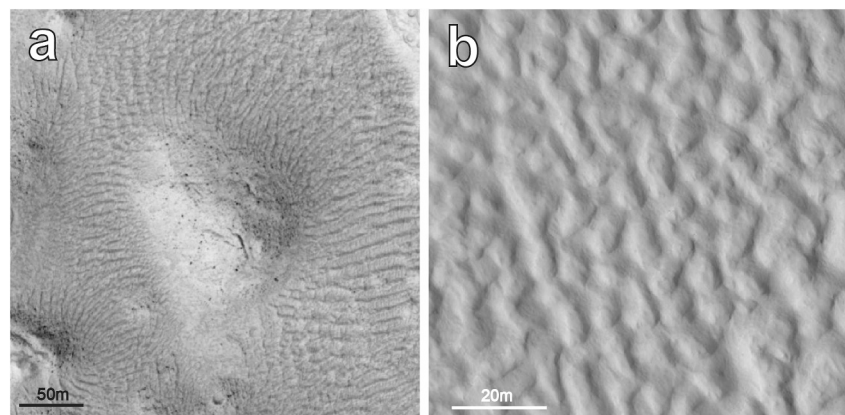

Figure 13. HiRISE images of characteristic landforms in 240°–300°E (northern Olympus Mons and Tempe Terra). (a) OSP-like fractured mound in Tempe Terra (ESP_015947_2210; 40.754°N, 297.501°E). (b) Brain terrains in Tempe Terra. (PSP_007667_2170; 36.734°N, 279.739°E).
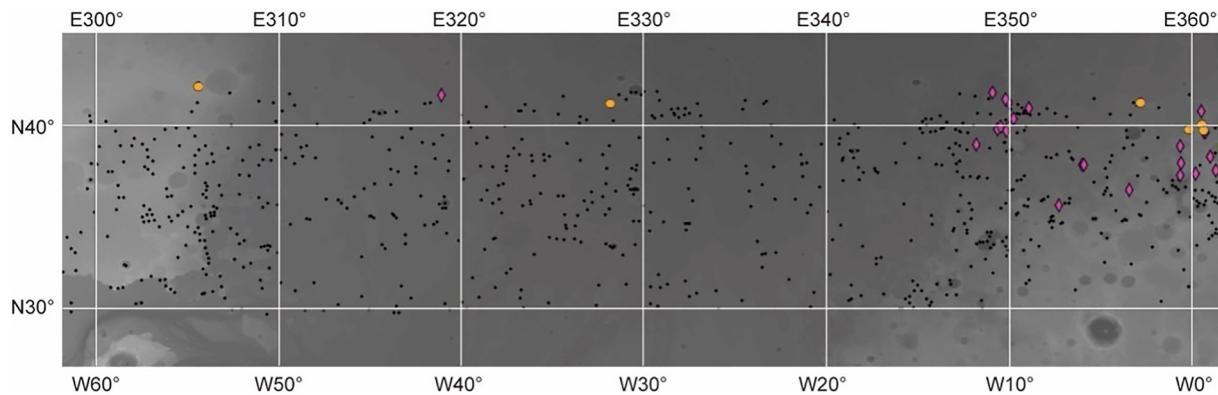
Figure 14. The distribution of target landforms from 300° to 360°E. This area is northern Chryse Planitia and southern Acidalia Planitia. This area is not distributed periglacial landforms like 240°to 300°E. Symbol legends are shown in Figure 4.

formed using a different process than the typical freeze-thaw process involved in the LCPs. On the other hand, the pronounced deep and elongated pits within the LMP rims (Figure 1e) are aligned along the N–S junction in polygonal margins (Séjourné et al., 2019). In the same longitudinal area of the 75°–105°E region, Séjourné et al. (2019) also documented the co-occurrence of large-sized polygons and elongated pits within the 38°–47°N latitudinal range, with scalloped depressions existing slightly more poleward within 42°–54°N. The morphology and collapse pattern of sinuous elongated pits, following polygonal cracks resemble degraded polygonal landforms on Bylot Island (Costard et al., 2016) and Ellesmere Island (Bernard-Grand'Maison & Pollard, 2018) in the Canadian Arctic Archipelago, and Tuktoyaktuk Coastlands of northern Canada (Soare et al., 2011), suggesting melting of subsurface ice and pooling in underground cavities. This evidence from the potential terrestrial analog sites of LMPs in the Arctic Archipelago and northern Canada implies that while significant ice existed during past high obliquity periods, much of it has likely degraded and dispersed over time. The absence of fresh icy craters (Dundas et al., 2021; Posiolova et al., 2022; Figure 16f) in this area also supports this interpretation.

Both CSP- and OSP-like fractured mounds exhibit a distribution pattern resembling polygons and brain terrain (Figures 16 and 17). OSP-type are more pronounced. Similar to a previous study (Dundas & McEwen, 2010), a notable concentration of fractured mounds was identified in the 0°–35°E and 65°–90°E regions. In addition, we recognized abundant fractured mounds within the 160°–230°E region, which had not been previously documented. Within the survey area, there are abundant occurrence of features such as fractured domes and mounds as well as flat textures. The coexisting domes, mounds, and flats are considered to be distinct evolutionary stages of pingos, similar to previous findings in Utopia and Elysium Planitia (de Pablo & Komatsu, 2009; Dundas & McEwen, 2010). It is noteworthy that CSP-type are not distributed in the areas of abundant LMPs occurrence in
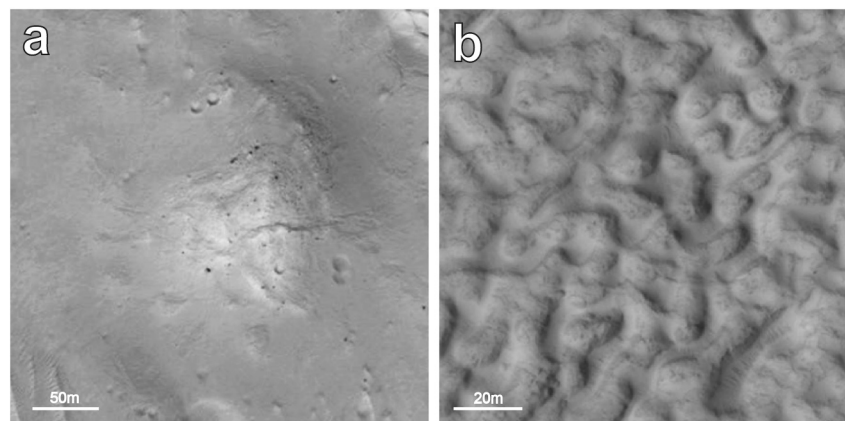

Figure 15. HiRISE images of characteristic landforms in 300°–360°E. (a) OSP-like fractured mound in northern Chryse Planitia (ESP_033102_2225; 42.18595°N, 305.712°E). (b) Brain terrains in northern Chryse Planitia (ESP_038032_2160; 38.6861°N, 352.8355°E).
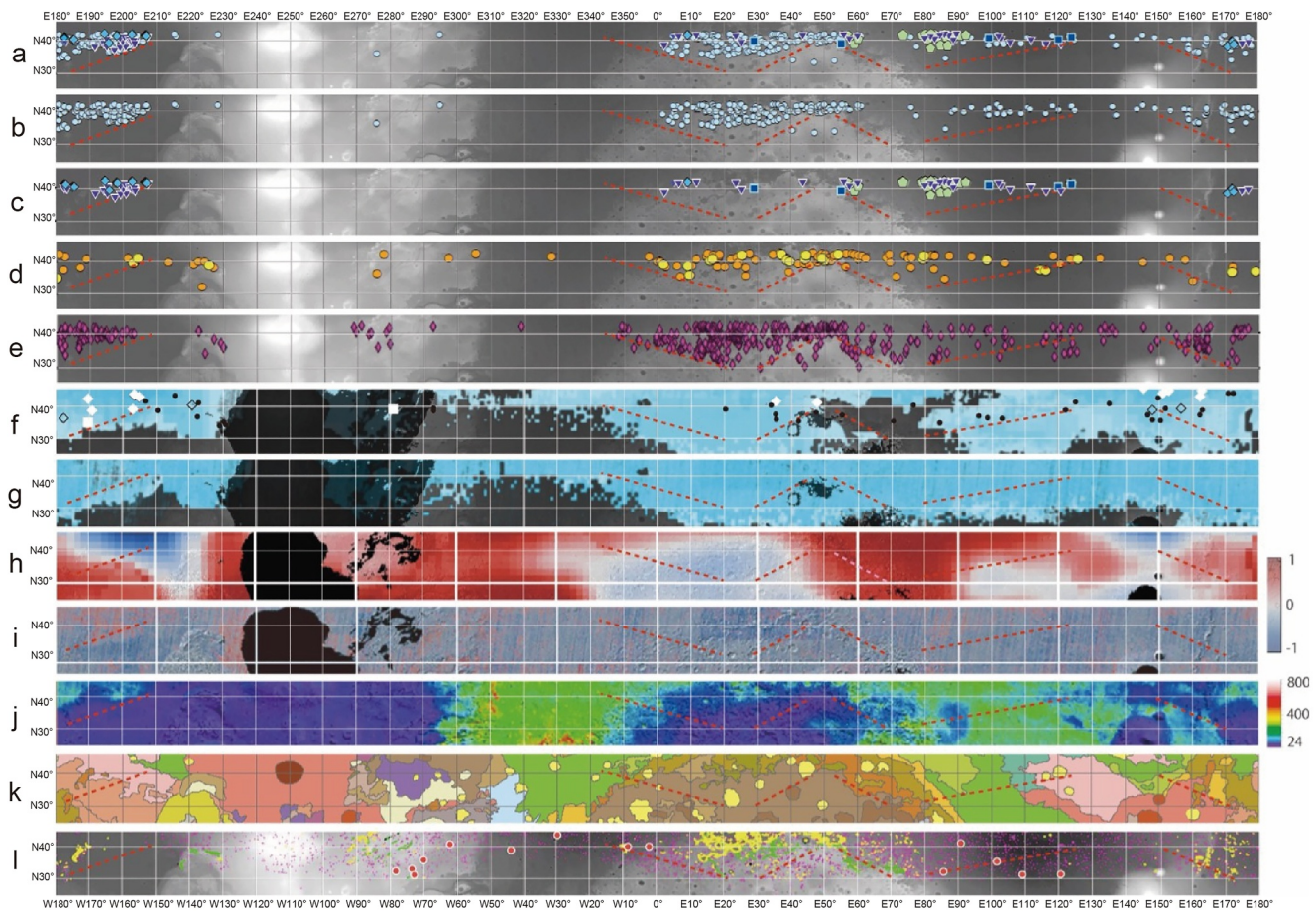
Figure 16. Comparison of the distribution of periglacial landforms obtained in this study (a)-(e) with various data sets (f–l). The red dotted line indicates the southern limit of periglacial landform distribution. The base map is MOLA shaded relief. (a) Distribution of all types of polygons. (b) Distribution of HCP. (c) Distribution of polygons excluding HCP. (d) Distribution of fractured mounds. (e) Distribution of brain terrain. (f) Subsurface ice consistency map of 0–1 m depth by the SWIM project (https://ammos.nasa.gov/marswatermaps/?mission=MWR). The white and black marks represent the distribution of ice-exposing craters (white points), possible ice-exposing craters (black open diamonds), and non-ice-exposing craters (black points) (Dundas et al., 2021; white circles: Posiolova et al., 2022; white quadrangle). (g) Subsurface ice consistency map of 1–5 m depth by SWIM project. (h) Neutron Data set representing the quantity of hydrogen (Feldman et al., 2011), illustrated as ice consistency map by SWIM project. (i) Rader Surface Power Return obtained from SHARAD surface output (Castaldo et al., 2017), illustrated as an ice consistency map by the SWIM project. (j) Thermal inertia data (Christensen et al., 2001). The regions of low thermal inertia are shown in blue, and the regions of high thermal inertia are shown in red. (k) Geologic map of surface geologic units on Mars (Tanaka et al., 2014). (l) Glacial landform distribution: LDA: yellow, LVF: light green, CCF: pink (Levy et al., 2014). The red circles indicate the distribution of post-glacial ice-free craters (Fassett et al., 2014).

Utopia Planitia, which is also consistent with the interpretation that subsurface ice in this area is currently degraded.

Although the formation mechanisms of brain terrains, especially their relationship with subsurface ice, are debated, we find the distribution of brain terrains to be consistent with those of thermal contraction polygons, fractured mounds, and ice-exposing craters. The southern extent of the distribution of brain terrain in mid-latitude Mars displays a zonal distribution with a sharp boundary with the surrounding terrain (Figure 16e). For instance, there is a WNW–ESE alignment spanning from 350°E, 40°N to 20°E, 30°N, followed by a WSW–ENE orientation from 30°E, 30°N to 50°E, 40°N, indicated by the red dotted line in Figure 16e. Similarly, there is a WNW–ESE orientation from 50°E, 40°N to 75°E, 30°N, a WSW–ENE orientation from 80°E, 30°N to 130°E, 40°N, a WNW–ESE orientation from 150°E, 40°N to 170°E, 30°N, and WSW–ENE orientation from 180°E, 30°N to 210°E, 40°N. It is noteworthy that the other two periglacial landforms (thermal contraction polygons and fractured mounds) are predominantly situated at latitudes higher than the zonal distribution of the brain terrain (Figures 16a–16e). This observation suggests that the brain terrain likely formed during an older period (higher obliquity condition) than the other two landforms.
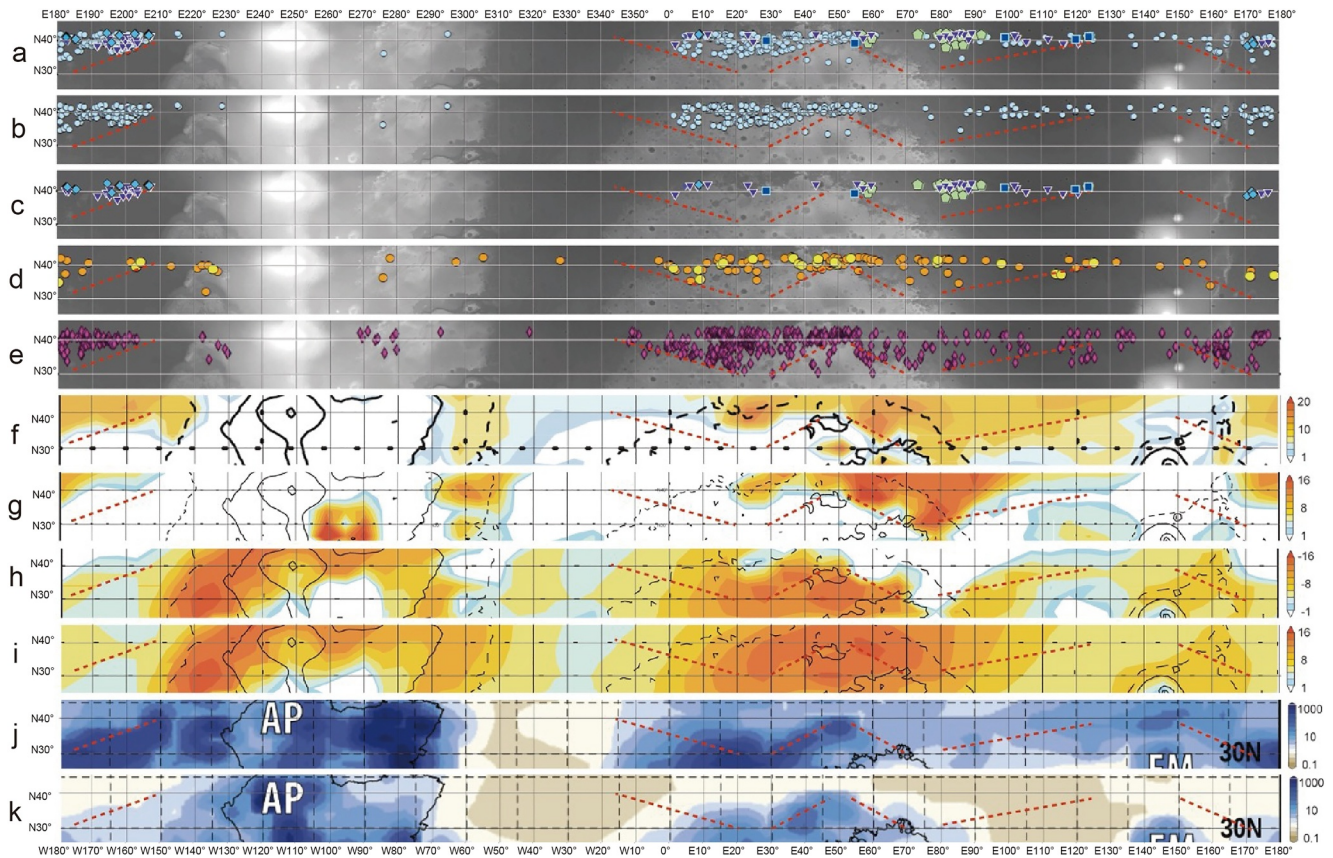
Figure 17. Comparison of the distribution of periglacial landforms obtained in this study (a–e) with various data sets (f–k). The red dotted line indicates the southern limit of periglacial landform distribution. The base map is MOLA shaded relief. (a) Distribution of all types of polygons. (b) Distribution of HCP. (c) Distribution of polygons excluding HCP. (d) Distribution of fractured mounds. (e) Distribution of brain terrain. (f) Annual subsurface water ice budget (mm/yr) at current obliquity 25° condition (Madeleine et al., 2009). (g) Annual subsurface water ice budget (mm/yr) at obliquity 35° condition (Madeleine et al., 2009). (h) Summer ice sublimation (mm) at obliquity 35° condition (Madeleine et al., 2009). (i) Winter ice accumulation (mm) at obliquity 35° condition (Madeleine et al., 2009). (j) Model-generated near-surface relative humidity in Northern hemisphere summer (Pál et al., 2019). (k) Model-generated near-surface relative humidity in Northern hemisphere winter (Pál et al., 2019).

4.2. Comparison With Other Existing Data Sets

To investigate the formational mechanisms of the three periglacial landforms, we conducted a comparative analysis using various data sets, including subsurface ice consistency maps obtained by the SWIM project (Figures 16f and 16g), neutron data set (Feldman et al., 2011; Figure 16h) and radar surface power return (Castaldo et al., 2017; Figure 16i) utilized in the SWIM project (Morgan et al., 2021). We also compared our results with thermal inertia data (Christensen et al., 2001; Figure 16j), a geological map (Tanaka et al., 2014; Figure 16k), and the occurrence of glacial-related landforms (LDA, LVF, CCF; Levy et al., 2014; Fassett et al., 2014; Figure 16l).

The distribution of the three periglacial landforms identified in our study roughly correlates with the recently updated subsurface ice consistency map of the SWIM project (Figures 16f and 16g). Interestingly, the 57°–92°E region where LMPs have developed corresponds to a less-ice area within the subsurface ice consistency map (at depth 0–1 m). However, there are significant differences between the southern limits of the three periglacial landforms and the subsurface ice consistency map. The SWIM results indicate the presence of ice (both depths of 0–1 m and 1–5 m) even where periglacial landforms are not distributed (Figures 16f and 16g). The difference between our survey results and the SWIM ice consistency map needs to be verified in the future after the SWIM project's original data of periglacial terrain distribution becomes publicly available.

On the other hand, the distribution of periglacial landforms does not align with the thermal inertia data (Christensen et al., 2001; Figure 16j), which can be indicative of surface material grain size (Fenton et al., 2003). This

suggests that variations in surface materials do not constrain the distribution of periglacial landforms. In addition, the distribution of these landforms does not match most of the geological units depicted on the geological map (Tanaka et al., 2014; Figure 16k), implying that geological classification does not influence their distribution significantly. This interpretation strengthens the interpretation that periglacial landform reflects subsurface ice conditions from the geologically young, that is, the latest Amazonian to the present day.

Comparison with the distribution of glacial landforms (LDA, LVF, CCF; Levy et al., 2014) reveals a correlation between the southern limit of LVF and brain terrain in the WSW–ENE orientation (20°–50°E area) as well as the WNW–ESE orientation (50°–75°E area) (Figure 16l). However, it is noteworthy that the distribution of LVF in specific longitudes (0°–20°E, 80°–130°E, 150°–170°E, and 180°–210°E) does not align with the southern limits of the brain terrain. In addition, the consistent occurrence of CCF north of 30°N and especially within 0°–190°E, 210°–310°E, and 340°–360°E longitude regions contrasts with the distribution pattern observed for the three periglacial landforms. This observation shows the idea that periglacial and glacial landforms likely represent different stages of subsurface ice development under the different climate regimes and boundary conditions. On the other hand, the distribution of LMPs correlates well with the distribution of post-glacial craters (Fassett et al., 2014) (Figure 16l). Post-glacial craters formed after the deposition of glacial materials and lack ice-rich fields, indicating that they likely developed after glacial retreat (Fassett et al., 2014). This finding supports our interpretation that LMPs represent a degraded form of subsurface ice.

4.3. Comparison With Climate Simulation Results

We compared our results with the annual water ice budgets (Madeleine et al., 2009) and seasonal variations in near-surface humidity (Daerden et al., 2019; Pál et al., 2019) available to date based on the general circulation models. Among the compared simulation data sets, the distribution of periglacial landforms obtained in our study demonstrates the highest consistency with the estimated annual water ice budget (Madeleine et al., 2009; Figures 17f–17i). Madeleine et al. (2009) examined the water ice budget over a year, focusing on the difference between the current obliquity of 25° condition and the past higher obliquity of 35°, coupled with different dust opacity levels (τdust = 1.5–2.5) (Figures 17f and 17g). They also evaluated the patterns of summer ice sublimation and winter ice accumulation during the 35° obliquity conditions (Figures 17h and 17i).

Our comparison between the distribution of periglacial landforms with model results utilizes a red dotted line as a reference to denote the southern limit (Figures 17f–17i). Notably, the map of the annual subsurface water ice budget in the current obliquity condition with high dust opacity shows the best alignment with the distribution of periglacial landforms (Figure 17f). Although some regions, such as the 295°–310°E area, showed a relatively high ice budget despite the absence of the three periglacial landforms, the distributions of these periglacial landforms and the annual ice budget are rather consistent. Particularly in regions of 10°–30°E, 65°–90°E and 160°–200°E, both the annual ice budgets (current obliquity condition) and the distribution of periglacial landforms extend southward, and the position of the red dotted line is well aligned (Figure 17f). On the other hand, the area of annual ice budgets under higher obliquity conditions exhibits a consistent but slightly reduced distribution (the southern limit of the ice budget area is distributed slightly north of the red dotted line; Figure 17g). Furthermore, it is noteworthy that the southern limit of this distribution closely corresponds to the boundary between regions dominated by intense summer ice sublimation (Figure 17h) and regions where this is less pronounced. However, the distribution of winter ice accumulation (Figure 17i) does not coincide with periglacial landforms, suggesting that the primary influence on its distribution is summer sublimation.

Regarding the area of 60°–100°E where LMPs are predominant, the present-day condition model (Figure 17f; Madeleine et al., 2009) indicates a lesser water ice budget compared to the past condition model (Figure 17g; Madeleine et al., 2009), implying that LMPs likely formed during the period of past intense ice accumulation activity under high obliquity. Therefore, we interpret the LMPs as the landforms formed in the past and are undergoing intense ice degradation. This interpretation is also consistent with the evidence from the potential terrestrial analog sites of LMPs in the Arctic Archipelago (Bylot Island: Costard et al., 2016; Ellesmere Island: Bernard-Grand'Maison & Pollard, 2018) and northern Canada (Tuktoyaktuk Coastlands: Soare et al., 2011), which implies that while significant ice existed there during past high-obliquity (>35°) periods, much of it has likely degraded over time (Séjourné et al., 2019; Soare et al., 2021; Ulrich et al., 2011).

We further compared our results with modeling results of seasonal variations in atmospheric water vapor and near-surface relative humidity. Daerden et al. (2019) presented the global seasonal variations of the atmospheric

water vapor by comparing the CRISM (Compact Reconnaissance Imaging Spectrometer for Mars; Murchie et al., 2007) data of H_2O absorption. Pál et al. (2019) further demonstrated the global seasonal variations of the near-surface relative humidity by utilizing the TES (Thermal Emission Spectrometer; Smith, 2004) data, with consideration of the topographic effect (Figures 17j and 17k). Since the areas of high near-surface relative humidity coincide with low thermal inertia features (Christensen et al., 2001; Figures 16j), Pál et al. (2019) interpreted that water vapor likely condenses in the near-surface atmosphere in these areas. It is noteworthy that areas of high near-surface humidity in both northern hemisphere summer and winter do not correspond to the distribution of periglacial landforms in this study, but rather to areas of low near-surface humidity (Figures 17j and 17k). The discrepancy between the distribution of periglacial landform and near-surface humidity suggests that there may be no interaction between the shallow subsurface ice and water vapor in the atmosphere. An alternative possibility is that in the southern part of the periglacial landforms, shallow subsurface ice is present in winter but sublimates in summer, which may indicate a consequent increase in atmospheric water vapor content as a result of sublimation. In this case, there may be an interaction between the distribution of shallow subsurface ice and the amount of atmospheric water vapor. Future verification for these two possibilities is desirable.

4.4. Possible Cause of the Distribution of Periglacial Landforms

There is regional heterogeneity in the longitudinal distribution of the periglacial landforms at latitudes 30°–42°N. This heterogenetic distribution pattern is consistent with the model-generated annual ice budget (Figure 17f; Madeleine et al., 2009). The primary cause of this variation can be attributed to the topographic forcing of stationary planetary waves and transient weather systems, caused by the Tharsis, Arabia, and Elysium mountains, as well as surface topography formed by bolide impacts (Neumann et al., 2004). The interaction between the Martian atmospheric circulation and the planet's topography might influence the regional heterogeneity in the distribution of the annual ice budget (Madeleine et al., 2009). These factors impact cloud formation and snowfall area, contributing to the distinct distribution of periglacial landforms.

We also considered factors beyond planetary waves and topographic forcing, such as volcanic influences (Butcher et al., 2017; Forget et al., 2006). Notably, Elysium Mons lies within 130°–150°E, while Aruba Mons occupies within 230°–270°E. A distinct circular pattern in the absence of periglacial landforms around these volcanic summits has been observed. This pattern could be attributed to either recent geothermal heat causing subsurface ice melting or the condition of surface volcanic sediments unsuitable for periglacial landform formation. Potential seismic activity has been indicated at Elysium Mons by InSight surveys, implying the occurrence of recent volcanic activity (Kedar et al., 2021). Additionally, Chryse Planitia at 290°–350°E exhibits the distribution of various edifice features possibly originating from sedimentary (mud) volcanoes (Brož et al., 2023; Komatsu et al., 2011, 2016). The condition prone to sedimentary volcanism may contribute to the absence of periglacial landforms in this region (e.g., sediment type, extrusion of subsurface water, and loss to the atmosphere).

5. Conclusions

We investigated the distribution of three presumed periglacial landforms (thermal contraction polygons, fractured mounds, and brain terrain) in the Martian mid-latitude region (30°–42°N) by observing 4,789 HiRISE images. We identified their distribution to occur mainly in the latitudes poleward of 35°N, especially within the regions of 0°–40°E, 60°–100°E, and 160°–210°E. Conversely, these landforms had a limited occurrence in the western hemisphere, particularly between 230° and 270°E and 280°–350°E. This comprehensive study reveals that the three landforms exhibit a consistent distribution pattern, implying a common origin involving ice-related processes.

We further conducted a classification of the polygons, identifying seven distinct types and mapping their occurrences. The majority of polygonal terrains within the 30°–42°N latitude range are High-Centered Polygons (HCPs), which coexist with other two periglacial landforms, except in the 60°–100°E region. Low-Centered Polygons (LCPs) and LCP–HCP Transitions (LHTs) are restricted at latitudes beyond 38°N, around 10°E, 30°E, 55°E, 100°E, 120°–124°E, 170°–173°E, and 180°–208°E, and closely corresponding to areas known to have recorded observations of fresh icy craters.

Large-sized Mixture Polygons (LMPs) exhibit a distinctive distribution, confined to 57°–92°E (i.e., western Utopia Planitia). The morphology and collapse patterns of sinuous elongated pits along the polygonal margins of

LMPs resemble degraded polygonal landforms found in terrestrial analogs of the Canadian Arctic Archipelago and northern Canada, indicating significant subsurface ice degradation. Climate models also suggest a reduced present-day water ice budget compared with periods of high obliquity in the past. Although substantial ice existed during past high-obliquity (>35°) periods, much of it has likely degraded over time in the LMP-dominant region between 57° and 92°E.

Based on findings from terrestrial analog studies which suggest that LCPs contain shallower subsurface ice than HCPs, it is implied that a substantial amount of subsurface ice may exist or have existed in areas where the LCPs and LHTs are present and where numerous polygons and fractured mounds are distributed (e.g., Amazonis Planitia, Arabia Terra, and eastern Utopia Planitia). These insights are also important when considering favorable landing sites for future human missions.

Data Availability Statement

All original data sets presented in this paper are available in an open-access repository (Sako et al., 2024; https://doi.org/10.6084/m9.figshare.26205488.v2).

References

Anglés, A., & Li, Y. (2017). The western Qaidam Basin as a potential Martian environmental analogue: An overview. *Journal of Geophysical Research: Planets*, *122*(5), 856–888. https://doi.org/10.1002/2017JE005293

Arvidson, R., Adams, D., Bonfiglio, G., Christensen, P., Cull, S., Golombek, M., et al. (2008). Mars Exploration Program 2007 Phoenix landing site selection and characteristics. *Journal of Geophysical Research*, *113*(E3). https://doi.org/10.1029/2007JE003021

Baker, D. M., Head, J. W., & Marchant, D. R. (2010). Flow patterns of lobate debris aprons and lineated valley fill north of Ismeniae Fossae, Mars: Evidence for extensive mid-latitude glaciation in the Late Amazonian. *Icarus*, *207*(1), 186–209. https://doi.org/10.1016/j.icarus.2009.11.017

Bernard-Grand'Maison, C., & Pollard, W. (2018). An estimate of ice wedge volume for a High Arctic polar desert environment, Fosheim Peninsula, Ellesmere Island. *The Cryosphere*, *12*(11), 3589–3604. https://doi.org/10.5194/tc-12-3589-2018

Bina, A., & Osinski, G. R. (2021). Decameter-scale rimmed depressions in Utopia Planitia: Insight into the glacial and periglacial history of Mars. *Planetary and Space Science*, *204*, 105253. https://doi.org/10.1016/j.pss.2021.105253

Brough, S., Hubbard, B., & Hubbard, A. (2016). Former extent of glacier-like forms on Mars. *Icarus*, *274*, 37–49. https://doi.org/10.1016/j.icarus.2016.03.006

Brough, S., Hubbard, B., & Hubbard, A. (2019). Area and volume of mid-latitude glacier-like forms on Mars. *Earth and Planetary Science Letters*, *507*, 10–20. https://doi.org/10.1016/j.epsl.2018.11.031

Brož, P., Oehler, D., Mazzini, A., Hauber, E., Komatsu, G., Etiope, G., & Cuřín, V. (2023). An overview of sedimentary volcanism on Mars. *Earth Surface Dynamics*, *11*(4), 633–661. https://doi.org/10.5194/esurf-11-633-2023

Buczkowski, D. L., Seelos, K. D., & Cooke, M. L. (2012). Giant polygons and circular graben in western Utopia basin, Mars: Exploring possible formation mechanisms. *Journal of Geophysical Research*, *117*(E8), E08010. https://doi.org/10.1029/2011JE003934

Burr, D. M., Tanaka, K. L., & Yoshikawa, K. (2009). Pingos on Earth and Mars. *Planetary and Space Science*, *57*(5–6), 541–555. https://doi.org/10.1016/j.pss.2008.11.003

Butcher, F. E., Balme, M. R., Gallagher, C., Arnold, N. S., Conway, S. J., Hagermann, A., & Lewis, S. R. (2017). Recent basal melting of a mid-latitude glacier on Mars. *Journal of Geophysical Research: Planets*, *122*(12), 2445–2468. https://doi.org/10.1002/2017JE005434

Castaldo, L., Mege, D., Gurgurewicz, J., Orosei, R., & Alberti, G. (2017). Global permittivity mapping of the Martian surface from SHARAD. *Earth and Planetary Science Letters*, *462*, 55–65. https://doi.org/10.1016/j.epsl.2017.01.012

Cheng, R. L., He, H., Michalski, J. R., & Li, Y. L. (2021b). A new type of polygonal terrain formed by sulfate weathering in arid regions. *Geomorphology*, *383*, 107695. https://doi.org/10.1016/j.geomorph.2021.107695

Cheng, R. L., He, H., Michalski, J. R., Li, Y. L., & Li, L. (2021a). Brain-terrain-like features in the Qaidam Basin: Implications for various morphological features on Mars. *Icarus*, *363*, 114434. https://doi.org/10.1016/j.icarus.2021.114434

Christensen, P. R., Morris, R. V., Lane, M. D., Bandfield, J. L., & Malin, M. C. (2001). Global mapping of Martian hematite mineral deposits: Remnants of water-driven processes on early Mars. *Journal of Geophysical Research*, *106*(E10), 23873–23885. https://doi.org/10.1029/2000JE001415

Costard, F., Séjourné, A., Kargel, J., & Godin, E. (2016). Modeling and observational occurrences of near-surface drainage in Utopia Planitia, Mars. *Geomorphology*, *275*, 80–89. https://doi.org/10.1016/j.geomorph.2016.09.034

Costard, F. M., & Kargel, J. S. (1995). Outwash plains and thermokarst on Mars. *Icarus*, *114*(1), 93–112. https://doi.org/10.1006/icar.1995.1046

Daerden, F., Neary, L., Viscardy, S., Muñoz, A. G., Clancy, R. T., Smith, M. D., et al. (2019). Mars atmospheric chemistry simulations with the GEM-Mars general circulation model. *Icarus*, *326*, 197–224. https://doi.org/10.1016/j.icarus.2019.02.030

Dafflon, B., Hubbard, S., Ulrich, C., Peterson, J., Wu, Y., Wainwright, H., & Kneafsey, T. J. (2016). Geophysical estimation of shallow permafrost distribution and properties in an ice-wedge polygon-dominated Arctic tundra region. *Geophysics*, *81*(1), WA247–WA263. https://doi.org/10.1190/geo2015-0175.1

Dang, Y. N., Xiao, L., Xu, Y., Zhang, F., Huang, J., Wang, J., et al. (2018). The polygonal surface structures in the Dalangtan playa, Qaidam Basin, NW China: Controlling factors for their formation and implications for analogous Martian landforms. *Journal of Geophysical Research: Planets*, *123*(7), 1910–1933. https://doi.org/10.1029/2018JE005525

de Pablo, M. Á., & Komatsu, G. (2009). Possible pingo fields in the Utopia basin, Mars: Geological and climatical implications. *Icarus*, *199*(1), 49–74. https://doi.org/10.1016/j.icarus.2008.09.007

Dickson, J. L., Head, J. W., & Fassett, C. I. (2012). Patterns of accumulation and flow of ice in the mid-latitudes of Mars during the Amazonian. *Icarus*, *219*(2), 723–732. https://doi.org/10.1016/j.icarus.2012.03.010

Dundas, C. M., Bramson, A. M., Ojha, L., Wray, J. J., Mellon, M. T., Byrne, S., et al. (2018). Exposed subsurface ice sheets in the Martian mid-latitudes. *Science*, *359*(6372), 199–201. https://doi.org/10.1126/science.aao1619

Dundas, C. M., Byrne, S., & McEwen, A. S. (2015). Modeling the development of Martian sublimation thermokarst landforms. *Icarus*, *262*, 154–169. https://doi.org/10.1016/j.icarus.2015.07.033

Dundas, C. M., & McEwen, A. S. (2010). An assessment of evidence for pingos on Mars using HiRISE. *Icarus*, *205*(1), 244–258. https://doi.org/10.1016/j.icarus.2009.02.020

Dundas, C. M., Mellon, M. T., Conway, S. J., Daubar, I. J., Williams, K. E., Ojha, L., et al. (2021). Widespread exposures of extensive clean shallow ice in the midlatitudes of Mars. *Journal of Geophysical Research: Planets*, *126*(3), e2020JE006617. https://doi.org/10.1029/2020JE006617

El-Maarry, M. R., Pommerol, A., & Thomas, N. (2013). Analysis of polygonal cracking patterns in chloride-bearing terrains on Mars: Indicators of ancient playa settings. *Journal of Geophysical Research: Planets*, *118*(11), 2263–2278. https://doi.org/10.1002/2013JE004463

El-Maarry, M. R., Watters, W., McKeown, N. K., Carter, J., Dobrea, E. N., Bishop, J. L., et al. (2014). Potential desiccation cracks on Mars: A synthesis from modeling, analogue-field studies, and global observations. *Icarus*, *241*, 248–268. https://doi.org/10.1016/j.icarus.2014.06.033

Fassett, C. I., Levy, J. S., Dickson, J. L., & Head, J. W. (2014). An extended period of episodic northern mid-latitude glaciation on Mars during the Middle to Late Amazonian: Implications for long-term obliquity history. *Geology*, *42*(9), 763–766. https://doi.org/10.1130/G35798.1

Feldman, P. D., Steffl, A. J., Parker, J. W., A'Hearn, M. F., Bertaux, J. L., Stern, S. A., et al. (2011). Rosetta-Alice observations of exospheric hydrogen and oxygen on Mars. *Icarus*, *214*(2), 394–399. https://doi.org/10.1016/j.icarus.2011.06.013

Fenton, L. K., Bandfield, J. L., & Ward, A. W. (2003). Aeolian processes in Proctor Crater on Mars: Sedimentary history as analyzed from multiple data sets. *Journal of Geophysical Research*, *108*(E12). https://doi.org/10.1029/2002JE002015

Forget, F., Haberle, R. M., Montmessin, F., Levrard, B., & Head, J. W. (2006). Formation of glaciers on Mars by atmospheric precipitation at high obliquity. *Science*, *311*(5759), 368–371. https://doi.org/10.1126/science.112033

Forget, F., Hourdin, F., Fournier, R., Hourdin, C., Talagrand, O., Collins, M., et al. (1999). Improved general circulation models of the Martian atmosphere from the surface to above 80 km. *Journal of Geophysical Research*, *104*(E10), 24155–24175. https://doi.org/10.1029/1999JE001025

Grosse, G., & Jones, B. M. (2011). Spatial distribution of pingos in northern Asia. *The Cryosphere*, *5*(1), 13–33. https://doi.org/10.5194/tc-5-13-2011

Head, J. W., Mustard, J. F., Kreslavsky, M. A., Milliken, R. E., & Marchant, D. R. (2003). Recent ice ages on Mars. *Nature*, *426*(6968), 797–802. https://doi.org/10.1038/nature02114

Hibbard, S. M., Williams, N. R., Golombek, M. P., Osinski, G. R., & Godin, E. (2021). Evidence for widespread glaciation in Arcadia Planitia, Mars. *Icarus*, *359*, 114298. https://doi.org/10.1016/j.icarus.2020.114298

Hiesinger, H., & Head III, J. W. (2000). Characteristics and origin of polygonal terrain in southern utopia Planitia, Mars: Results from Mars orbiter Laser Altimeter and Mars orbiter camera data. *Journal of Geophysical Research*, *105*(E5), 11999–12022. https://doi.org/10.1029/1999JE001193

Holt, J. W., Safaeinili, A., Plaut, J. J., Head, J. W., Phillips, R. J., Seu, R., et al. (2008). Radar sounding evidence for buried glaciers in the southern mid-latitudes of Mars. *Science*, *322*(5905), 1235–1238. https://doi.org/10.1126/science.1164246

Ishikawa, M., & Yamkhin, J. (2016). Formation chronology of Arsain pingo, Darhad basin, northern Mongolia. *Permafrost and Periglacial Processes*, *27*(3), 297–306. https://doi.org/10.1002/ppp.1877

Jones, B. M., Grosse, G., Hinkel, K. M., Arp, C. D., Walker, S., Beck, R. A., & Galloway, J. P. (2012). Assessment of pingo distribution and morphometry using an IfSAR derived digital surface model, western Arctic Coastal Plain, Northern Alaska. *Geomorphology*, *138*, 1–14. https://doi.org/10.1016/j.geomorph.2011.08.007

Kedar, S., Panning, M. P., Smrekar, S. E., Stähler, S. C., King, S. D., Golombek, M. P., et al. (2021). Analyzing low frequency seismic events at Cerberus Fossae as long period volcanic quakes. *Journal of Geophysical Research: Planets*, *126*(4), e2020JE006518. https://doi.org/10.1029/2020JE006518

Komatsu, G., Okubo, C. H., Wray, J. J., Ojha, L., Cardinale, M., Murana, A., et al. (2016). Small edifice features in Chryse Planitia, Mars: Assessment of a mud volcano hypothesis. *Icarus*, *268*, 56–75. https://doi.org/10.1016/j.icarus.2015.12.032

Komatsu, G., Ori, G. G., Cardinale, M., Dohm, J. M., Baker, V. R., Vaz, D. A., et al. (2011). Roles of methane and carbon dioxide in geological processes on Mars. *Planetary and Space Science*, *59*(2–3), 169–181. https://doi.org/10.1016/j.pss.2010.07.002

Komatsu, G., Ori, G. G., Marinangeli, L., & Moersch, J. E. (2007). Playa environments on Earth: Possible analogs for Mars. ISBN: 9780521832922. In M. G. Chapman (Ed.), *The Geology of Mars: Evidence from Earth-based analogs* (pp. 322–348). Cambridge University Press.

Kress, A. M., & Head, J. W. (2008). Ring-mold craters in lineated valley fill and lobate debris aprons on Mars: Evidence for subsurface glacial ice. *Geophysical Research Letters*, *35*(23). https://doi.org/10.1029/2008GL035501

Laskar, J., Correia, A. C., Gastineau, M., Joutel, F., Levrard, B., & Robutel, P. (2004). Long term evolution and chaotic diffusion of the insolation quantities of Mars. *Icarus*, *170*(2), 343–364. https://doi.org/10.1016/j.icarus.2004.04.005

Levy, J., Head, J., & Marchant, D. (2009a). Thermal contraction crack polygons on Mars: Classification, distribution, and climate implications from HiRISE observations. *Journal of Geophysical Research*, *114*(E1). https://doi.org/10.1029/2008JE003273

Levy, J., Head, J., & Marchant, D. (2009b). Concentric crater fill in Utopia Planitia: History and interaction between glacial "brain terrain" and periglacial mantle processes. *Icarus*, *202*, 462–476. https://doi.org/10.1016/j.icarus.2009.02.018

Levy, J., Head, J. W., & Marchant, D. R. (2010b). Concentric crater fill in the northern mid-latitudes of Mars: Formation processes and relationships to similar landforms of glacial origin. *Icarus*, *209*(2), 390–404. https://doi.org/10.1016/j.icarus.2010.03.036

Levy, J. S., Fassett, C. I., Head, J. W., Schwartz, C., & Watters, J. L. (2014). Sequestered glacial ice contribution to the global Martian water budget: Geometric constraints on the volume of remnant, midlatitude debris-covered glaciers. *Journal of Geophysical Research: Planets*, *119*(10), 2188–2196. https://doi.org/10.1002/2014JE004685

Levy, J. S., Marchant, D. R., & Head, J. W. (2010a). Thermal contraction crack polygons on Mars: A synthesis from HiRISE, Phoenix, and terrestrial analog studies. *Icarus*, *206*(1), 229–252. https://doi.org/10.1016/j.icarus.2009.09.005

Liljedahl, A. K., Boike, J., Daanen, R. P., Fedorov, A. N., Frost, G. V., Grosse, G., et al. (2016). Pan-Arctic ice-wedge degradation in warming permafrost and its influence on tundra hydrology. *Nature Geoscience*, *9*(4), 312–318. https://doi.org/10.1038/NGEO2674

Mackay, J. R. (1998). Pingo growth and collapse, Tuktoyaktuk Peninsula area, western Arctic coast, Canada: A long-term field study. *Géographie Physique et Quaternaire*, *52*(3), 271–323. https://doi.org/10.7202/004847ar

Mackay, J. R. (1999). Periglacial features developed on the exposed lake bottoms of seven lakes that drained rapidly after 1950, Tuktoyaktuk Peninsula area, western Arctic coast, Canada. *Permafrost and Periglacial Processes*, *10*(1), 39–63. https://doi.org/10.1002/(SICI)1099-1530(199901/03)10:1<39::AID-PPP305>3.0.CO;2-R

Madeleine, J. B., Forget, F., Head, J. W., Levrard, B., Montmessin, F., & Millour, E. (2009). Amazonian northern mid-latitude glaciation on Mars: A proposed climate scenario. *Icarus*, *203*(2), 390–405. https://doi.org/10.1016/j.icarus.2009.04.037

Malin, M. C., Bell III, J. F., Cantor, B. A., Caplinger, M. A., Calvin, W. M., Clancy, R. T., et al. (2007). Context camera investigation on board the Mars reconnaissance orbiter. *Journal of Geophysical Research*, *112*(E5). https://doi.org/10.1029/2006JE002808

Mangold, N. (2003). Geomorphic analysis of lobate debris aprons on Mars at Mars Orbiter Camera scale: Evidence for ice sublimation initiated by fractures. *Journal of Geophysical Research*, *108*(E4), 8021. https://doi.org/10.1029/2002JE001885

Mangold, N. (2005). High latitude patterned grounds on Mars: Classification, distribution and climatic control. *Icarus*, *174*(2), 336–359. https://doi.org/10.1016/j.icarus.2004.07.030

Marchant, D. R., & Head III, J. W. (2007). Antarctic dry valleys: Microclimate zonation, variable geomorphic processes, and implications for assessing climate change on Mars. *Icarus*, *192*(1), 187–222. https://doi.org/10.1016/j.icarus.2007.06.018

Marchant, D. R., Lewis, A. R., Phillips, W. M., Moore, E. J., Souchez, R. A., Denton, G. H., et al. (2002). Formation of patterned ground and sublimation till over Miocene glacier ice in Beacon Valley, southern Victoria Land, Antarctica. *Geological Society of America Bulletin*, *114*(6), 718–730. https://doi.org/10.1130/0016-7606(2002)114<0718:FOPGAS>2.0.CO;2

Matsuoka, N. (2011). Climate and material controls on periglacial soil processes: Toward improving periglacial climate indicators. *Quaternary Research*, *75*(2), 356–365. https://doi.org/10.1016/j.yqres.2010.12.014

Matsuoka, N., Christiansen, H. H., & Watanabe, T. (2018). Ice-wedge polygon dynamics in Svalbard: Lessons from a decade of automated multi-sensor monitoring. *Permafrost and Periglacial Processes*, *29*(3), 210–227. https://doi.org/10.1002/ppp.1985

McEwen, A. S., Eliason, E. M., Bergstrom, J. W., Bridges, N. T., Hansen, C. J., Delamere, W. A., et al. (2007). Mars reconnaissance orbiter's high resolution imaging science experiment (HiRISE). *Journal of Geophysical Research*, *112*(E5). https://doi.org/10.1029/2005JE002605

Mellon, M. T., Arvidson, R. E., Marlow, J. J., Phillips, R. J., & Asphaug, E. (2008). Periglacial landforms at the Phoenix landing site and the northern plains of Mars. *Journal of Geophysical Research*, *113*, E00A23. https://doi.org/10.1029/2007JE003039

Mellon, M. T., Arvidson, R. E., Sizemore, H. G., Searls, M. L., Blaney, D. L., Cull, S., et al. (2009a). Ground ice at the Phoenix landing site: Stability state and origin. *Journal of Geophysical Research*, *114*(E1). https://doi.org/10.1029/2009JE003417

Mellon, M. T., Malin, M. C., Arvidson, R. E., Searls, M. L., Sizemore, H. G., Heet, T. L., et al. (2009b). The periglacial landscape at the Phoenix landing site. *Journal of Geophysical Research*, *114*(E1). https://doi.org/10.1029/2009JE003418

Morgan, G. A., Putzig, N. E., Perry, M. R., Sizemore, H. G., Bramson, A. M., Petersen, E. I., et al. (2021). Availability of subsurface water-ice resources in the northern mid-latitudes of Mars. *Nature Astronomy*, *5*(3), 230–236. https://doi.org/10.1038/s41550-020-01290-z

Murchie, S., Arvidson, R., Bedini, P., Beisser, K., Bibring, J. P., Bishop, J., et al. (2007). Compact reconnaissance imaging spectrometer for Mars (CRISM) on Mars reconnaissance orbiter (MRO). *Journal of Geophysical Research*, *112*(E5). https://doi.org/10.1029/2006JE002682

Murton, J. (2013). Permafrost and periglacial features| ice wedges and ice-wedge casts. *Encyclopedia of Quaternary Science*, *3*, 436–451. https://doi.org/10.1016/b978-0-444-53643-3.00097-2

Murton, J. B., Worsley, P., & Gozdzik, J. (2000). Sand veins and wedges in cold aeolian environments. *Quaternary Science Reviews*, *19*(9), 899–922. https://doi.org/10.1016/S0277-3791(99)00045-1

Neumann, G. A., Zuber, M. T., Wieczorek, M. A., McGovern, P. J., Lemoine, F. G., & Smith, D. E. (2004). Crustal structure of Mars from gravity and topography. *Journal of Geophysical Research*, *109*(E8), E08002. https://doi.org/10.1029/2004JE002262

Osterloo, M. M., Hamilton, V. E., Bandfield, J. L., Glotch, T. D., Baldridge, A. M., Christensen, P. R., et al. (2008). Chloride-bearing materials in the southern highlands of Mars. *Science*, *319*(5870), 1651–1654. https://doi.org/10.1126/science.1150690

Pál, B., Kereszturi, Á., Forget, F., & Smith, M. D. (2019). Global seasonal variations of the near-surface relative humidity levels on present-day Mars. *Icarus*, *333*, 481–495. https://doi.org/10.1016/j.icarus.2019.07.007

Plaut, J. J., Safaeinili, A., Holt, J. W., Phillips, R. J., Head III, J. W., Seu, R., et al. (2009). Radar evidence for ice in lobate debris aprons in the mid-northern latitudes of Mars. *Geophysical Research Letters*, *36*(2), L02203. https://doi.org/10.1029/2008GL036379

Posiolova, L., Lognonné, P., Banerdt, W. B., Clinton, J., Collins, G. S., Kawamura, T., et al. (2022). Largest recent impact craters on Mars: Orbital imaging and surface seismic co-investigation. *Science*, *378*(6618), 412–417. https://doi.org/10.1126/science.abq7704

Sako, T., Hasegawa, H., Ruj, T., Komatsu, G., & Sekine, Y. (2024). Original data for Sako et al. JGR Planets [Datasets]. *figshare*. https://doi.org/10.6084/m9.figshare.26205488.v2

Seibert, N. M., & Kargel, J. S. (2001). Small-scale Martian polygonal terrain: Implications for liquid surface water. *Geophysical Research Letters*, *28*(5), 899–902. https://doi.org/10.1029/2000GL012093

Séjourné, A., Costard, F., Gargani, J., Soare, R. J., Fedorov, A., & Marmo, C. (2011). Scalloped depressions and small-sized polygons in western Utopia Planitia, Mars: A new formation hypothesis. *Planetary and Space Science*, *59*(5–6), 412–422. https://doi.org/10.1016/j.pss.2011.01.007

Séjourné, A., Costard, F., Swirad, Z. M., Łosiak, A., Bouley, S., Smith, I., et al. (2019). Grid mapping the Northern Plains of Mars: Using morphotype and distribution of ice-related landforms to understand multiple ice-rich deposits in Utopia Planitia. *Journal of Geophysical Research: Planets*, *124*(2), 483–503. https://doi.org/10.1029/2018JE005665

Sinha, R. K., & Vijayan, S. (2017). Geomorphic investigation of craters in Alba Mons, Mars: Implications for late Amazonian glacial activity in the region. *Planetary and Space Science*, *144*, 32–48. https://doi.org/10.1016/j.pss.2017.05.014

Sletten, R. S., Hallet, B., & Fletcher, R. C. (2003). Resurfacing time of terrestrial surfaces by the formation and maturation of polygonal patterned ground. *Journal of Geophysical Research*, *108*(E4), 8044. https://doi.org/10.1029/2002JE001914

Smith, D. E., Zuber, M. T., Frey, H. V., Garvin, J. B., Head, J. W., Muhleman, D. O., et al. (2001). Mars orbiter laser altimeter: Experiment summary after the first year of global mapping of Mars. *Journal of Geophysical Research*, *106*(E10), 23689–23722. https://doi.org/10.1029/2000JE001364

Smith, M. D. (2004). Interannual variability in TES atmospheric observations of Mars during 1999–2003. *Icarus*, *167*(1), 148–165. https://doi.org/10.1016/j.icarus.2003.09.010

Soare, R. J., Burr, D. M., & Tseung, J. M. W. B. (2005). Possible pingos and a periglacial landscape in northwest Utopia Planitia. *Icarus*, *174*(2), 373–382. https://doi.org/10.1016/j.icarus.2004.11.013

Soare, R. J., Conway, S. J., & Dohm, J. M. (2014a). Possible ice-wedge polygons and recent landscape modification by "wet" periglacial processes in and around the Argyre impact basin, Mars. *Icarus*, *233*, 214–228. https://doi.org/10.1016/j.icarus.2014.01.034

Soare, R. J., Conway, S. J., Dohm, J. M., & El-Maarry, M. R. (2014b). Possible open-system (hydraulic) pingos in and around the Argyre impact region of Mars. *Earth and Planetary Science Letters*, *398*, 25–36. https://doi.org/10.1016/j.epsl.2014.04.044

Soare, R. J., Conway, S. J., Pearce, G. D., Dohm, J. M., & Grindrod, P. M. (2013). Possible crater-based pingos, paleolakes and periglacial landscapes at the high latitudes of Utopia Planitia, Mars. *Icarus*, *225*(2), 971–981. https://doi.org/10.1016/j.icarus.2012.08.041

Soare, R. J., Conway, S. J., Williams, J. P., Gallagher, C., & Mc Keown, L. E. (2020). Possible (closed system) pingo and ice-wedge/thermokarst complexes at the mid latitudes of Utopia Planitia, Mars. *Icarus*, *342*, 113233. https://doi.org/10.1016/j.icarus.2019.03.010

Soare, R. J., Conway, S. J., Williams, J. P., Philippe, M., Mc Keown, L. E., Godin, E., & Hawkswell, J. (2021). Possible ice-wedge polygonisation in Utopia Planitia, Mars and its latitudinal gradient of distribution. *Icarus*, *358*, 114208. https://doi.org/10.1016/j.icarus.2020.114208

Soare, R. J., Osinski, G. R., & Roehm, C. L. (2007). Thermokarst lakes and ponds on Mars in the very recent (late Amazonian) past. *Earth and Planetary Science Letters*, *272*(1–2), 382–393. https://doi.org/10.1016/j.epsl.2008.05.010

Soare, R. J., Séjourné, A., Pearce, G., Costard, F., & Osinski, G. R. (2011). The Tuktoyaktuk Coastlands of northern Canada: A possible "wet" periglacial analog of Utopia Planitia, Mars. *Geological Society of America Special Paper*, *483*, 203–218. https://doi.org/10.1130/2011.2483(13)

Souness, C., Hubbard, B., Milliken, R. E., & Quincey, D. (2012). An inventory and population-scale analysis of Martian glacier-like forms. *Icarus*, *217*(1), 243–255. https://doi.org/10.1016/j.icarus.2011.10.020

Squyres, S. W. (1979). The distribution of lobate debris aprons and similar flows on Mars. *Journal of Geophysical Research*, *84*(B14), 8087–8096. https://doi.org/10.1029/JB084iB14p08087

Squyres, S. W., & Carr, M. H. (1986). Geomorphic evidence for the distribution of ground ice on Mars. *Science*, *231*(4735), 249–252. https://doi.org/10.1126/science.231.4735.249

Tanaka, K. L., Robbins, S. J., Fortezzo, C. M., Skinner Jr, J. A., & Hare, T. M. (2014). The digital global geologic map of Mars: Chronostratigraphic ages, topographic and crater morphologic characteristics, and updated resurfacing history. *Planetary and Space Science*, *95*, 11–24. https://doi.org/10.1016/j.pss.2013.03.006

Ulrich, M., Hauber, E., Herzschuh, U., Härtel, S., & Schirrmeister, L. (2011). Polygon pattern geomorphometry on Svalbard (Norway) and western Utopia Planitia (Mars) using high-resolution stereo remote-sensing data. *Geomorphology*, *134*(3–4), 197–216. https://doi.org/10.1016/j.geomorph.2011.07.002

Xiao, L., Wang, J., Dang, Y., Cheng, Z., Huang, T., Zhao, J., et al. (2017). A new terrestrial analogue site for Mars research: The Qaidam Basin, Tibetan Plateau (NW China). *Earth-Science Reviews*, *164*, 84–101. https://doi.org/10.1016/j.earscirev.2016.11.003